



ATLAS CONF Note

ATLAS-CONF-2018-028

5th July 2018



Measurements of Higgs boson properties in the diphoton decay channel using 80 fb^{-1} of pp collision data at $\sqrt{s} = 13 \text{ TeV}$ with the ATLAS detector

The ATLAS Collaboration

This note reports measurements of Higgs boson properties in the two-photon final state using 79.8 fb^{-1} of data recorded at $\sqrt{s} = 13 \text{ TeV}$ by the ATLAS experiment at the Large Hadron Collider. The cross sections of Higgs boson production through gluon–gluon fusion, vector-boson fusion, and in association with a vector boson or a top-quark pair are measured. Measurements of the Higgs boson production divided further into kinematic regions, called simplified template cross sections, are also reported. Additionally, the cross section for the production of the Higgs boson decaying to two isolated photons is measured in a fiducial phase space designed to closely match the ATLAS detector acceptance, and is found to be $60.4 \pm 6.1 \text{ (stat.)} \pm 6.0 \text{ (exp.)} \pm 0.3 \text{ (theo.) fb}$, in agreement with the Standard Model prediction of $63.5 \pm 3.3 \text{ fb}$. Finally, the fiducial cross section is measured differentially in bins of several kinematic observables with sensitivity to properties of the Higgs boson. Among these, the number of b -jets produced in association with the Higgs boson is measured to probe Higgs production in association with heavy flavor hadrons. No significant deviations between the observed data and the Standard Model prediction are observed.



1 Introduction

In 2012, the ATLAS [1] and CMS [2] collaborations announced the discovery of the Higgs boson [3, 4]. Subsequent measurements have sought to characterize the properties of the Higgs boson and its production mechanisms. This year (2018), the observation of Higgs boson production in association with a top quark pair was reported by both CMS and ATLAS [5, 6]. Higgs boson properties have been previously measured in the diphoton decay channel at $\sqrt{s} = 13$ TeV [7, 8]; in 2017, ATLAS recorded an additional 43.6 fb^{-1} of good quality data, allowing for roughly a 50% improvement in statistical precision compared to the previous measurement [7].

This note reports measurements of the properties of the Higgs boson decaying to two photons, using 79.8 fb^{-1} of pp collision data collected by the ATLAS detector between 2015 and 2017. The cross sections of the Higgs production modes are measured inclusively and in kinematic phase space regions known as simplified template cross sections (STXS) [9, 10]. The cross section is also measured inclusively in a fiducial phase space designated to match the selection at reconstruction level, and corrected for detector effects to the particle level. Within this phase space, the Higgs boson signal is measured differentially in bins of kinematic observables that shed light on its properties. In addition, the number of b -jets is measured in a fiducial region containing one or more central jets and no electrons or muons, in order to probe Higgs boson production in association with heavy-flavor hadrons (excluding $t\bar{t}H$). All measurements are compared to Standard Model (SM) theoretical predictions.

The measurements presented in this note follow a methodology that is largely unchanged since Ref. [7]; differences are highlighted in the text. A notable exception is the re-optimization of the measurement of the top-associated production mode, which is documented as part of the ATLAS observation of $t\bar{t}H$ production [6] and summarized in this note. Despite sharing the same methodology and data set, the measurement of the $t\bar{t}H$ production mode in this note differs from Ref. [6] due to a different treatment of the other production modes, which were fixed to the SM prediction in Ref. [6] and are fit to data here, and due to different effects of the systematic uncertainties derived from the fit of additional categories. The fiducial measurement of the number of b -jets is also new in this note.

The note is organized as follows. The remainder of this section introduces the general analysis strategy. Section 2 briefly describes the ATLAS detector, and Section 3 defines the data set used for these results. Section 4 describes the simulated samples used for the measurements. Section 5 outlines the procedure to reconstruct objects and events in the data set. The modeling of signal and background processes and the statistical methods used for interpreting the results are described in Section 6. The systematic uncertainties are described in Section 7. The results of the production mode and simplified template cross section measurements are reported in Section 8, and findings of the inclusive fiducial and differential cross section measurements are reported in Section 9. Section 10 summarizes the main conclusions of the results.

1.1 Higgs boson production mode cross sections and simplified template cross sections

In this note, for Higgs boson absolute rapidity¹ $|y_H| < 2.5$, cross sections are measured for several production modes of the Higgs boson: gluon–gluon fusion (ggF), vector-boson fusion (VBF), Higgs boson production in association with a vector boson (VH : sum of WH , $q\bar{q}' \rightarrow ZH$, and $gg \rightarrow ZH$ processes), and Higgs boson production in association with a top–antitop quark pair ($t\bar{t}H$) or a single top quark (tH : sum of t -channel process tHq and W -associated process tHW). Higgs boson production in association with a bottom–antibottom quark pair ($b\bar{b}H$) is merged with ggF, because it is expected to have small contributions, and similar kinematics and acceptance to ggF. In addition, the signal strength, defined as the ratio of the observed to expected event yield, is measured for inclusive Higgs production.

Furthermore, the simplified template cross sections introduced in Refs. [9, 10] are investigated. For $|y_H| < 2.5$, the different Higgs boson production modes are separated into fiducial regions of phase space using the kinematics and topology of the final state, defined by the Higgs boson, the vector bosons or top quarks, and the hadronic jets in the event. The SM predictions of the Higgs boson production modes are used as “templates” for those fiducial regions. The template cross section measurements are designed to proceed in stages: “stage 0” is defined using the five main production modes (ggF, VBF, VH (leptonic decays), top-associated production, and $b\bar{b}H$); “stage 1” divides these regions further based on event kinematic properties, to be measured when the experimental sensitivity allows. In the simplified template cross section framework, the WH and $q\bar{q}' \rightarrow ZH$ processes with the vector boson decaying hadronically are grouped with the VBF production mode, and the $gg \rightarrow ZH$ process with the Z boson decaying hadronically is grouped with the ggF production mode. This organization is different from the one used in the production mode cross section measurements. Additionally, because the current data set is not large enough to probe all 31 stage-1 cross sections, regions with poor sensitivity or with large anti-correlations are merged together, such that 9 cross section regions are measured.

Figure 1 and Table 1 summarize the stage-0 and stage-1 cross sections relevant to this measurement and indicate the 9 measured cross sections. The diphoton events are divided into 29 categories based on the reconstructed event properties, to target the different production modes and the different simplified template cross section regions. These event reconstruction categories are also shown in Figure 1, and discussed in Section 8.

1.2 Fiducial integrated and differential cross sections

The $pp \rightarrow H \rightarrow \gamma\gamma$ cross section is measured in a fiducial region matching the selection imposed at reconstruction level and reported both as an integrated cross section and in differential measurements. The *diphoton fiducial region* used for the inclusive measurement is defined at the particle level by requiring two photons, not originating from hadrons, that are each required to have an absolute pseudorapidity $|\eta| < 2.37$ and outside the region $1.37 < |\eta| < 1.52$. The two photons with the highest transverse momenta define the diphoton system. The leading (subleading) photon must have a transverse momentum greater than 35% (25%) of the mass of the diphoton system, $m_{\gamma\gamma}$. Both photons must be isolated from other activity using a particle-level isolation requirement. The kinematic and isolation requirements of

¹ The ATLAS experiment uses a right-handed coordinate system with its origin at the nominal interaction point (IP) in the center of the detector and the z -axis along the beam pipe. The x -axis points from the IP to the center of the LHC ring, and the y -axis points upward. Cylindrical coordinates (r, ϕ) are used in the transverse plane, ϕ being the azimuthal angle around the z -axis. The pseudorapidity is defined in terms of the polar angle θ as $\eta = -\ln \tan(\theta/2)$. When dealing with massive particles, the rapidity $y = 1/2 \ln[(E + p_z)/(E - p_z)]$ is used, where E is the energy and p_z is the z -component of the momentum.

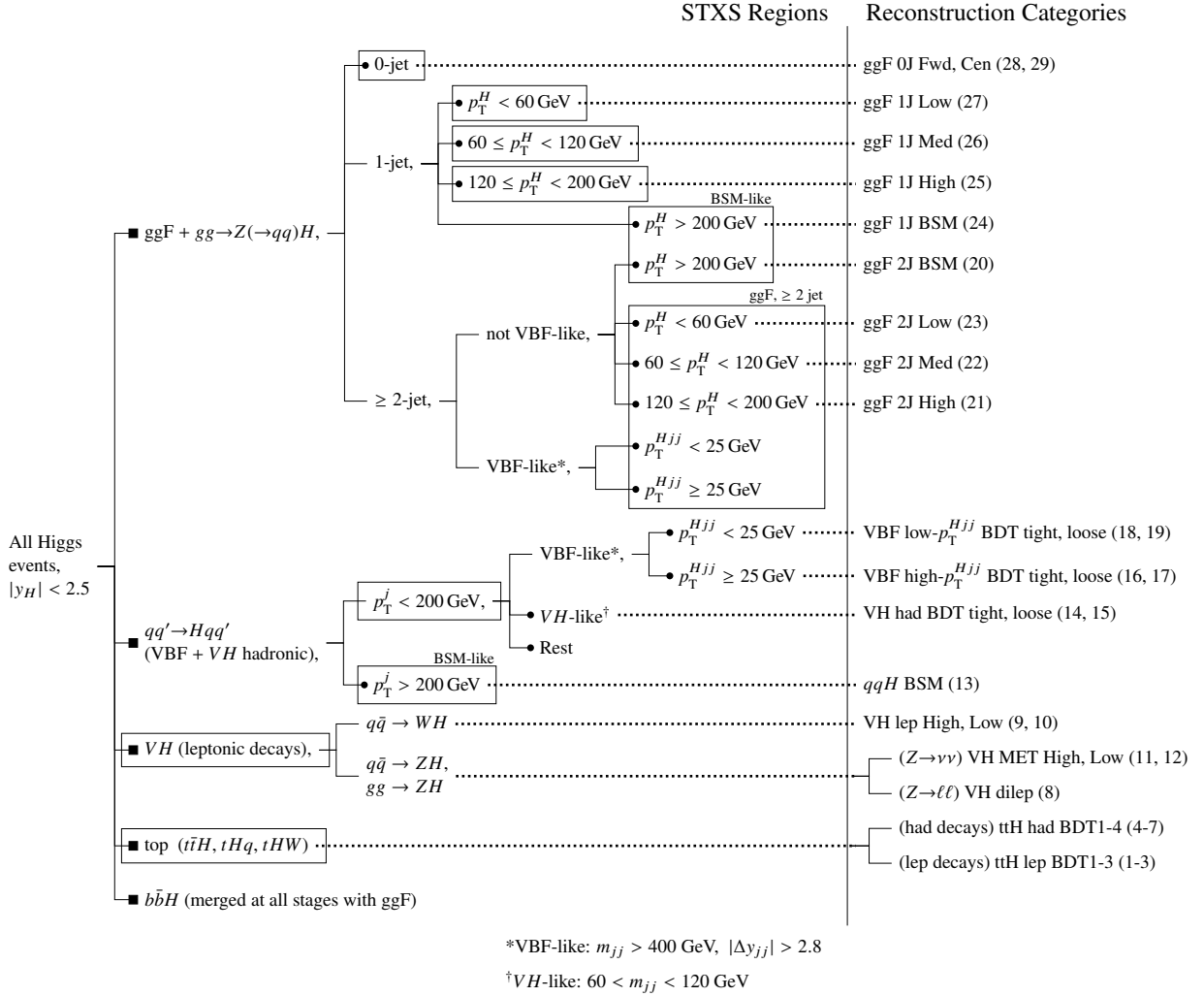


Figure 1: The particle-level kinematic regions relevant to this measurement, as defined by the simplified template cross section (STXS) framework. Stage-0 simplified template cross section regions are indicated with an adjacent square; stage-1 regions are denoted with a circle. Some stage-1 regions are omitted from the figure in cases where the data set lacks the sensitivity to resolve them. The event reconstruction categories targeting specific particle-level kinematic regions, defined in Table 3, are listed to the right of each region. Events in data are assigned preferentially to categories starting from “ttH lep BDT1” and using the order indicated by the numbers in parentheses (note that the ggF categories are mutually exclusive of one another). Though some of the non- $t\bar{t}H$ category names have changed, the definition of those categories is the same as in Ref. [7]. The particle-level regions are merged to form 9 intermediate regions, indicated with rectangular boxes, whose cross sections are measured in this note. Note that one disjoint region (“BSM-like”) is denoted by two labeled boxes.

Process	Measurement region	Stage-1 region
$ggF + gg \rightarrow Z(\rightarrow qq)H$	0-jet	0-jet
	1-jet, $p_T^H < 60$ GeV	1-jet, $p_T^H < 60$ GeV
	1-jet, $60 \leq p_T^H < 120$ GeV	1-jet, $60 \leq p_T^H < 120$ GeV
	1-jet, $120 \leq p_T^H < 200$ GeV	1-jet, $120 \leq p_T^H < 200$ GeV
	BSM-like* (\geq 1-jet, $p_T^H > 200$ GeV)	1-jet, $p_T^H > 200$ GeV \geq 2-jet, $p_T^H > 200$ GeV
	\geq 2 jet ($p_T^H < 200$ GeV or VBF-like)	\geq 2-jet, $p_T^H < 60$ GeV \geq 2-jet, $60 \leq p_T^H < 120$ GeV \geq 2-jet, $120 \leq p_T^H < 200$ GeV VBF-like, $p_T^{Hjj} < 25$ GeV VBF-like, $p_T^{Hjj} \geq 25$ GeV
$qq' \rightarrow Hqq'$ (VBF + VH hadronic)	$p_T^j < 200$ GeV	$p_T^j < 200$ GeV, VBF-like, $p_T^{Hjj} < 25$ GeV $p_T^j < 200$ GeV, VBF-like, $p_T^{Hjj} \geq 25$ GeV $p_T^j < 200$ GeV, VH -like $p_T^j < 200$ GeV, Rest
	BSM-like* ($p_T^j > 200$ GeV)	$p_T^j > 200$ GeV
VH (leptonic decays)	VH leptonic	$q\bar{q} \rightarrow ZH, p_T^Z < 150$ GeV
		$q\bar{q} \rightarrow ZH, 150 \text{ GeV} < p_T^Z < 250$ GeV, 0-jet
		$q\bar{q} \rightarrow ZH, 150 \text{ GeV} < p_T^Z < 250$ GeV, \geq 1-jet
		$q\bar{q} \rightarrow ZH, p_T^Z > 250$ GeV
		$q\bar{q} \rightarrow WH, p_T^W < 150$ GeV
		$q\bar{q} \rightarrow WH, 150 \text{ GeV} < p_T^W < 250$ GeV, 0-jet
		$q\bar{q} \rightarrow WH, 150 \text{ GeV} < p_T^W < 250$ GeV, \geq 1-jet
		$q\bar{q} \rightarrow WH, p_T^W > 250$ GeV
		$gg \rightarrow ZH, p_T^Z < 150$ GeV
		$gg \rightarrow ZH, p_T^Z > 150$ GeV, 0-jet
		$gg \rightarrow ZH, p_T^Z > 150$ GeV, \geq 1-jet
top-associated production	Top	$t\bar{t}H$
		tHW
		$tHqb$
$b\bar{b}H$	merged w/ ggF	$b\bar{b}H$

Table 1: The kinematic regions of the stage-1 simplified template cross sections. The left column indicates the five main production modes, the middle column describes the 9 measurements probed in this result, and the right column lists the stage-1 template cross sections and their relation to the measurements. Note that the cross section of the sum of the two measurement regions labeled “BSM-like” (marked with an asterisk) is reported. All regions require $|y_H| < 2.5$. Jets are defined using the anti- k_t algorithm with radius parameter $R = 0.4$ and are required to have $p_T > 30$ GeV. The leading jet and Higgs boson transverse momenta are denoted by p_T^j and p_T^H , respectively. The transverse momentum of the Higgs boson and the leading and subleading jet is denoted as p_T^{Hjj} . Events are considered “VBF-like” if they contain at least two jets with an invariant mass of $m_{jj} > 400$ GeV and a rapidity separation between the two jets of $|\Delta y_{jj}| > 2.8$. Events are considered “ VH -like” if they contain at least two jets with an invariant mass of $60 \text{ GeV} < m_{jj} < 120$ GeV. All $qq' \rightarrow Hqq'$ VBF and VH events (with the vector boson V decaying hadronically) which are neither VBF nor VH -like are part of the “Rest” selection.

the fiducial selection are defined to mimic the event selection imposed on data in order to minimize any uncertainty associated with extrapolating outside the detector fiducial volume. Electrons, muons and jets are also defined at the particle level as described in detail in Section 9.

Using the diphoton fiducial region defined above, the following distributions are measured differentially at the particle level:

- $p_T^{\gamma\gamma}$, the transverse momentum of the diphoton system,
- $|y_{\gamma\gamma}|$, the rapidity of the diphoton system,
- $p_T^{j_1}$, the transverse momentum of the leading jet,
- $N_{b\text{-jets}}$, the number of central jets² containing a b -hadron, in a fiducial region described below.

The distribution of $N_{b\text{-jets}}$ is measured in a fiducial region designed to probe Higgs boson production in association with heavy-flavor particles, which is poorly constrained theoretically, and which is an important background in measurements and searches for $t\bar{t}H$ and HH production. In order to specifically target Higgs boson production in association with heavy-flavor particles and reduce the fraction of $t\bar{t}H$ events, the fiducial region for this measurement is constructed using a veto on electrons and muons. In addition, at least one central jet with transverse momentum $p_T > 30$ GeV is required to match the acceptance of the inner detector.

2 ATLAS detector

The ATLAS detector [1] covers almost the entire solid angle around the proton–proton interaction point. It consists of an inner tracking detector, electromagnetic and hadronic calorimeters, and a muon spectrometer.

The inner detector (ID), immersed in a 2 T axial magnetic field provided by a superconducting solenoid, provides precision tracking for charged particles ($|\eta| < 2.5$). The ID consists of a silicon pixel detector (including the insertable B-layer [11]), a silicon microstrip detector (SCT), and a transition radiation tracker (TRT). The ID is surrounded by the electromagnetic (EM) and hadronic calorimeters. The EM calorimeter is a lead/liquid-argon (LAr) sampling calorimeter, measuring electromagnetic showers in the barrel ($|\eta| < 1.475$) and endcap ($1.375 < |\eta| < 3.2$) regions. The hadronic calorimeter reconstructs hadronic showers using steel and scintillator tiles ($|\eta| < 1.7$), copper/LAr ($1.5 < |\eta| < 3.2$), or copper–tungsten/LAr ($3.1 < |\eta| < 4.9$). A muon spectrometer (MS) surrounds the calorimeter system. It comprises separate trigger chambers ($|\eta| < 2.4$) and precision tracking chambers ($|\eta| < 2.7$), in a magnetic field provided by three superconducting air-core toroids.

ATLAS data-taking uses a two-level trigger system [12]: a hardware-based first-level (L1) trigger component, reducing the event rate to at most 100 kHz, and a software-based high-level trigger component, reducing the event rate to approximately 1 kHz.

² Central jets are defined as having $|y| < 2.5$, matching the acceptance of the inner detector.

3 Data set

This study uses a data set of $\sqrt{s} = 13$ TeV proton-proton collisions recorded by the ATLAS detector from 2015 to 2017. After data quality requirements are applied to ensure good working condition of all detector components, the data set amounts to an integrated luminosity of $79.8 \pm 1.6 \text{ fb}^{-1}$. The mean number of interactions per bunch crossing was on average $\langle\mu\rangle = 24$ combining data collected in 2015 and 2016, and in 2017 it increased to $\langle\mu\rangle = 38$. Events are selected by a diphoton trigger with transverse energy thresholds of 35 GeV and 25 GeV for the leading and subleading photon candidates, respectively. The photon identification requirements of this trigger were tightened in 2017 to cope with a higher instantaneous luminosity. On average, the trigger has an efficiency greater than 98% for events that pass the diphoton event selection described in Section 5.

4 Event simulation

Signal events from ggF, VBF, VH , $t\bar{t}H$ and $b\bar{b}H$ production modes are generated using POWHEG [13–20], with the PDF4LHC15 PDF set [21], and interfaced to PYTHIA8 [22, 23] for parton showering, hadronization and underlying event using the AZNLO set of parameters that are tuned to data [24]. tH processes are modeled using MADGRAPH5_AMC@NLO [25] with the CT10 PDF set [26]. tHq events are passed to PYTHIA8 with the A14 parameter set [27], while tHW events are interfaced to HERWIG++ [28–30] with the HERWIG++ UEEE5 parameter set. The generated signal events are passed through a GEANT4 [31] simulation of the ATLAS detector response. The cross sections of Higgs production processes are reported for a center-of-mass energy of $\sqrt{s} = 13$ TeV and a SM Higgs with mass 125.09 GeV. These cross sections [9, 32–49], along with the Higgs branching ratio to diphotons (0.227%) [9, 50–54], are used to normalize the simulated signal events.

Background events from continuum $\gamma\gamma$ production and $V\gamma\gamma$ production are generated using SHERPA 2.2.4 [55], and merged with the SHERPA parton shower [56] according to the ME+PS@NLO prescription [57]. The CT10 PDF set and dedicated parton shower tuning developed by the SHERPA authors are used. $t\bar{t}\gamma\gamma$ production is modeled using MADGRAPH5_AMC@NLO interfaced to PYTHIA8, with the PDF4LHC15 PDF set and the A14 parameter set. The background samples are passed through a fast parametric simulation of the ATLAS detector response [58].

Additional proton-proton interactions (pile-up) are produced using PYTHIA8 with the A2 parameter set [59] and the MSTW2008LO PDF set [60]. They are included in the simulation for all generated events such that the distribution of the mean number of interactions per bunch crossing reproduces that observed in the data.

A summary of the simulated signal and background samples is shown in Table 2.

5 Event reconstruction and selection

Collision events are reconstructed in the ATLAS detector using a series of object reconstruction algorithms, summarized below. Events in this analysis are selected using the following procedure: first, reconstructed photon candidates are required to satisfy a set of *preselection*-level identification criteria. The two highest- p_T preselected photons are used to define the diphoton system, and an algorithm is used

Process	Generator	Showering	PDF set	σ [pb] $\sqrt{s} = 13$ TeV	Order of σ calculation
ggF	POWHEG NNLOPS	PYTHIA 8	PDF4LHC15	48.52	N ³ LO(QCD)+NLO(EW)
VBF	POWHEG-Box	PYTHIA 8	PDF4LHC15	3.78	approximate-NNLO(QCD)+NLO(EW)
WH	POWHEG-Box	PYTHIA 8	PDF4LHC15	1.37	NNLO(QCD)+NLO(EW)
$q\bar{q}' \rightarrow ZH$	POWHEG-Box	PYTHIA 8	PDF4LHC15	0.76	NNLO(QCD)+NLO(EW)
$gg \rightarrow ZH$	POWHEG-Box	PYTHIA 8	PDF4LHC15	0.12	NNLO(QCD)+NLO(EW)
$t\bar{t}H$	POWHEG-Box	PYTHIA 8	PDF4LHC15	0.51	NNLO(QCD)+NLO(EW)
$b\bar{b}H$	POWHEG-Box	PYTHIA 8	PDF4LHC15	0.49	NNLO(QCD)+NLO(EW)
tHq	MG5_AMC@NLO	PYTHIA 8	CT10	0.07	4FS(LO)
$tH\bar{W}$	MG5_AMC@NLO	Herwig++	CT10	0.02	5FS(NLO)
$\gamma\gamma$	SHERPA	SHERPA	CT10		
$V\gamma\gamma$	SHERPA	SHERPA	CT10		
$t\bar{t}\gamma\gamma$	MG5_AMC@NLO	PYTHIA 8	PDF4LHC15		

Table 2: Event generators and PDF sets used to model signal and background processes. The cross sections of Higgs production processes [9, 32–49] are reported for a center of mass energy of $\sqrt{s} = 13$ TeV and a SM Higgs with mass 125.09 GeV. The order of the calculated cross section is reported in each case. The cross sections for the background processes are omitted, because the background normalisation is determined in fits to the data.

to select the *diphoton primary vertex* among the reconstructed vertices. Finally, the photons are required to satisfy isolation and additional identification selection criteria. Additional objects (jets, muons, electrons, and missing energy) are also reconstructed and identified for the purpose of further categorizing the events and measuring Higgs boson properties.

5.1 Photon reconstruction and identification

Photons are reconstructed from calorimeter clusters formed using a dynamical, topological cell clustering-based algorithm [61, 62]. The photon candidate is classified as *converted* if two tracks forming a conversion vertex, or one track with the signature of an electron track but without hits in the innermost pixel layer, are matched to it; otherwise it is labeled as *unconverted*. The photon candidate energy is calibrated using a procedure developed in Run 1 [63] and re-optimized for 13 TeV data [64].

Reconstructed photons must satisfy $|\eta| < 2.37$ in order to fall inside the region of the EM calorimeter with a finely segmented layer, and outside the range $1.37 < |\eta| < 1.52$ corresponding to the transition region of the barrel and endcap EM calorimeters. Photon candidates are separated from jet backgrounds using an identification criteria based on calorimeter shower shape variables [61, 65]. A *loose* working point is used for preselection, and the final selection of photon candidates is made using a *tight* selection. For photons above 25 GeV, the efficiency of the *tight* identification ranges from about 84% to 94% (85% to 98%) for unconverted photons (converted photons).

The final selection of photons includes calorimeter- and track-based isolation requirements to further suppress jets misidentified as photons. The calorimeter isolation variable is defined as the energy in the EM calorimeter in a radius $\Delta R = 0.2$ around the photon candidate, excluding the energy associated to the photon candidate and correcting for pile-up and underlying event contributions [65, 66]. The calorimeter-based isolation must be less than 6.5% of the photon transverse energy for each photon candidate. The track-based isolation variable is defined as the scalar sum of the transverse momenta of tracks with a radius $\Delta R < 0.2$ around the photon candidate. The tracks considered in the isolation variable are restricted to those with $p_T > 1$ GeV that are associated to the selected diphoton primary vertex and not associated

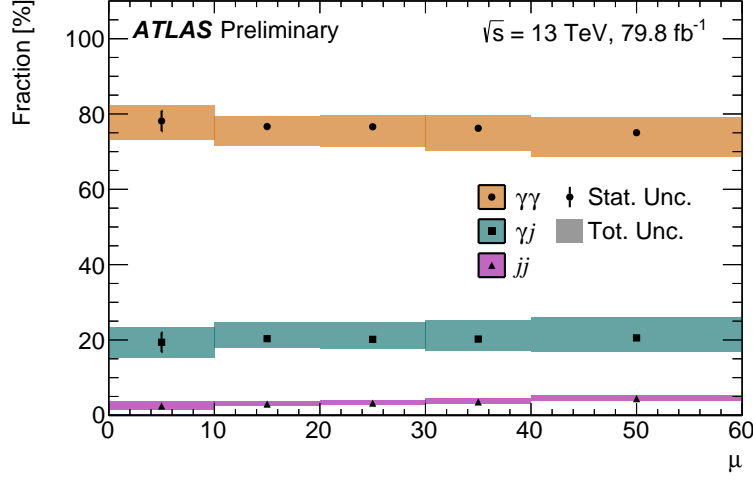


Figure 2: The purity of $\gamma\gamma$ events in the diphoton fiducial region, measured in bins of μ (the mean number of interactions per bunch crossing). The fraction of $\gamma\gamma$, γj and $j j$ events in each μ region is measured using the procedure described in Section 6.2.

with a photon conversion vertex. Both photons must have a track isolation less than 5% of the photon transverse energy.

5.2 Event selection and selection of the diphoton primary vertex

Events are selected by first requiring at least two photons satisfying the *loose* identification preselection criteria. The two highest- p_T preselected photons are designated as the candidates for the diphoton system, and all other photon candidates are discarded. The measured trajectory of these two photons, along with the reconstructed vertex information in the event, are used as inputs to a neural-network algorithm trained on simulation to determine the correct primary vertex [67]. This algorithm has been shown to select the correct primary vertex (within 0.3 mm of the true vertex) in simulated gluon-fusion signal events 76% of the time. Its performance was validated using $Z \rightarrow ee$ events in data and simulation, ignoring the track information of the electrons and treating them as photon candidates [68]. The two preselected photon candidates are required to satisfy the *tight* identification criteria and the isolation selection described above. Finally, the leading and subleading photon candidates are required to satisfy $p_T/m_{\gamma\gamma} > 0.35$ and 0.25, respectively.

The trigger, object and event selection described up until now are used to define the events that are selected for further analysis for Higgs boson properties. In total, 733455 events are selected in this data set with a diphoton invariant mass between 105 and 160 GeV. The predicted signal efficiency, assuming a SM Higgs boson and including the fiducial acceptance of the kinematic selection, is 34%.

With respect to the previous analysis, which used data collected in 2015 and 2016, the additional data collected in 2017 features higher pile-up conditions. Despite this increase in pile-up, the purity of $\gamma\gamma$ events with respect to events with one or two jets reconstructed as photons is fairly stable. Figure 2 illustrates the purity of $\gamma\gamma$ events in bins of μ as measured by the background composition procedure described in Section 6.2.

5.3 Reconstruction and selection of hadronic jets, b -jets, leptons and missing transverse momentum

Jets are reconstructed from topological clusters in the calorimeters using the anti- k_t algorithm with radius parameter 0.4 [69]. Jets are required to have $|\eta| < 4.4$, as well as $p_T > 25$ or 30 GeV depending on the measurement performed. Jets originating from pile-up collisions in the range $|\eta| < 2.4$ and $p_T < 60$ GeV are suppressed using a jet vertex tagger multivariate discriminant [70, 71]. Jets with $|\eta| < 2.5$ containing b -hadrons are identified using the MV2c10 b -tagging algorithm with a working point selected to achieve a 70% or 77% b -tagging efficiency [72, 73] depending on the measurement.

Electrons are constructed by matching tracks in the ID to topological calorimeter clusters formed using the same dynamical, topological cell clustering-based algorithm as in the photon reconstruction [62, 74]. Electron candidates are required to have $p_T > 10$ GeV, $|\eta| < 2.47$ and must satisfy a selection based on a likelihood discriminant made from calorimeter shower shapes and track parameters [75]. Isolation criteria are applied to electrons using calorimeter- and track-based information using a selection designed to obtain a flat efficiency of 99% in all ranges of η and p_T . The reconstructed track associated to the electron candidate must be consistent with the diphoton vertex by requiring its longitudinal impact parameter z_0 relative to the vertex to satisfy $|z_0 \sin \theta| < 0.5$ mm. In addition, the electron transverse impact parameter with respect to the beam axis divided by its uncertainty, $|d_0|/\sigma_{d_0}$, must be less than 5.

Muons are reconstructed by matching tracks from the MS and ID subsystems. Muons without an ID track but whose MS track is compatible with the interaction point are also considered. Muon candidates are required to have $p_T > 10$ GeV, $|\eta| < 2.7$, and must satisfy the *medium* identification requirements [76]. Muons are required to satisfy calorimeter- and track-based isolation requirements that are 95-97% efficient for muons with $p_T \in [10, 60]$ GeV and 99% efficient for $p_T > 60$ GeV. Muon tracks must satisfy $|z_0 \sin \theta| < 0.5$ mm and $|d_0|/\sigma_{d_0} < 3$.

An overlap removal procedure is performed in order to avoid double-counting objects, using the quantity $\Delta R = \sqrt{\Delta\phi^2 + \Delta y^2}$. First, electrons overlapping with the two selected photons ($\Delta R < 0.4$) are removed. Jets overlapping with the selected photons ($\Delta R < 0.4$) and electrons ($\Delta R < 0.2$) are removed. Electrons overlapping with the remaining jets ($\Delta R < 0.4$) are removed to match the requirements imposed when measuring isolated electron efficiencies. Finally, muons overlapping with photons or jets ($\Delta R < 0.4$) are removed.

The missing transverse momentum is defined as the negative vector sum of the transverse momenta of the selected photon, electron, muon and jet objects, as well as of the transverse momenta of remaining low- p_T particles estimated using tracks associated to the primary vertex but not assigned to any of the above selected objects [77].

6 Signal and background modeling

The Higgs boson signal yield is extracted using a maximum likelihood fit to the diphoton invariant mass spectrum in each event reconstruction category and differential cross-section bin, and in the diphoton fiducial region (which are defined in Sections 8 and 9). The fit is performed on data in the range $105 < m_{\gamma\gamma} < 160$ GeV using parameterized models for signal and background. The signal and background modeling follows the methodology described in Ref. [7] and is summarized below.

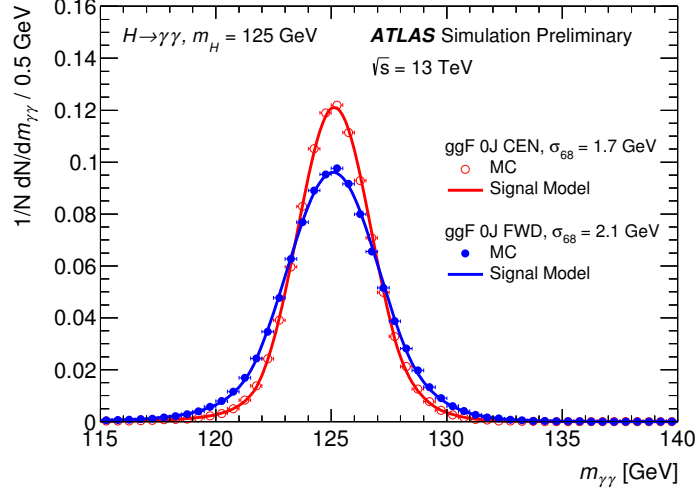


Figure 3: Simulated signal events and the fitted signal parameterization for two event categories. The ggF 0J Cen category has among the best mass resolutions, and the ggF 0J Fwd region has the worst mass resolution of the measured categories.

6.1 Signal model

The Higgs boson signal is modeled as a double-sided Crystal Ball function, with the bulk of the distribution modeled by a Gaussian distribution and upper and lower tails described using power-law functions [78, 79]. The parameters of the signal model are obtained using a fit to the simulated Higgs samples in each differential bin and event reconstruction category, and in the diphoton fiducial region. Figure 3 depicts the signal model parameterizations for two event categories having among the best (ggF 0J Cen), and the worst (ggF 0J Fwd) mass resolutions. The effective signal mass resolutions of these categories, defined as half the smallest $m_{\gamma\gamma}$ window containing 68% of signal events, are 1.7 and 2.1 GeV, respectively. Table 11 in the appendix reports the effective signal mass resolutions in all 29 reconstruction categories.

6.2 Background model and composition

The background is modeled in each event region or category using either a power law function, a fourth-order Bernstein polynomial, or an exponential of a first-, second-, or third-order polynomial. Background functions are chosen in each region to ensure a small potential bias on the measured signal yield while keeping the number of degrees of freedom small to reduce the statistical uncertainty. The procedure to measure the possible bias, and thus to make the choice of function, is performed using fits of the signal plus background model to a sample representing the background-only invariant mass spectrum.

The background samples used to perform the bias tests and determine the background functional form are taken from data control regions or simulated samples, depending on the region. For fiducial differential bins, ggF categories, VBF categories, and VH hadronic categories, which are dominated by $\gamma\gamma$, γj and jj backgrounds, the simulated SHERPA $\gamma\gamma$ events are used as a background model. This sample is corrected

to reflect the shape differences of γj and jj and taking into account the relative event fractions of $\gamma\gamma$, γj and jj in each region.

To measure the relative $\gamma\gamma$, γj and jj event fractions in each region, a double two-dimensional sideband method [66, 80] is applied using data control regions in which the nominal identification and isolation requirements are relaxed. To determine the shape difference between SHERPA $\gamma\gamma$ and γj , the simulated $\gamma\gamma$ shape is compared to a control region in which the identification criteria of exactly one of the two photons is inverted; contamination from $\gamma\gamma$ in this region is subtracted, and a linear reweighting is derived to match the $\gamma\gamma$ and control region shapes. The procedure is repeated in a control region in which the identification criteria of both photons is inverted to determine a shape reweighting for jj events. These derived shapes are combined with the measured relative event fractions to obtain the total background shape. In the inclusive sample of selected events with diphoton invariant mass between 105 and 160 GeV, the $\gamma\gamma$ fraction is measured to be $75.6^{+3.1}_{-4.8}\%$; the error is dominated by the systematic uncertainty. Figure 2 in Section 5 reports the purity of $\gamma\gamma$ events in bins of the mean number of interactions per bunch crossing.

Background templates for categories targeting VH signal decaying to charged or neutral leptons are obtained using simulated $V\gamma\gamma$ and $\gamma\gamma$ background samples, combined according to the predicted cross sections. Categories targeting leptonic tH and $t\bar{t}H$ decay modes use simulated $t\bar{t}\gamma\gamma$ samples to model the background.

For categories targeting tH and $t\bar{t}H$ production with hadronically decaying top quarks, data control regions are obtained using events in which at least one of the two photons fails either isolation or identification selection criteria, and the requirement on the number of b -tagged jets is removed, but satisfying all other selection criteria. These templates are validated by verifying that their shape describes the data in the diphoton invariant mass ranges $105 < m_{\gamma\gamma} < 120$ GeV and $130 < m_{\gamma\gamma} < 160$ GeV of the signal region.

In each category or region, signal plus background fits are performed on the background-only templates described above using candidate background functions and the parameterized signal model. The absolute value of the amount of signal fitted in a signal plus background fit is a measure of the potential bias caused by the choice of background function. The maximum of this quantity from a series of fits scanning the parameterized signal mass in the range 121-129 GeV, called the *spurious signal*, is the metric used to describe the systematic uncertainty due to the choice of background function.

If the spurious signal of a background function is less than 10% of the expected SM Higgs yield, or less than 20% of the expected error on the measured signal yield, or if the spurious signal is consistent with satisfying one of these criteria within 2σ of the statistical uncertainty on the estimated spurious signal, then the function is considered as a background model. The statistical uncertainty on the estimated spurious signal is caused by the finite size of the background sample used to perform the test. Furthermore, a background-only fit of the function to the background sample must satisfy a loose χ^2 requirement, $p(\chi^2) > 0.01$.³ Among the functions satisfying these criteria in a given region or category, the function with the smallest number of parameters is chosen. In case two candidate functions have the same number of parameters, the function with the smallest spurious signal is chosen. The selected functions have between 1 and 4 degrees of freedom (excluding the parameter used to normalize to data), depending on the category, bin, or region.

³ In a few differential bins and categories, $p(\chi^2)$ requirement fails for all candidate functions due to random fluctuations in the background sample. The requirement is dropped in these individual cases.

6.3 Statistical Model

The statistical procedure used to interpret the data is described in Ref. [81] and follows the methods from Ref. [7]. For each measurement, signal yields are determined using the maximum profile likelihood ratio for an extended likelihood function. The likelihood functions used in each measurement are described below.

For the inclusive fiducial measurement, the likelihood function is built from the diphoton invariant mass distribution of data events in the range $m_{\gamma\gamma} \in [105, 160]$ GeV and satisfying the diphoton fiducial region requirements. The signal and background parameterizations determined for the inclusive measurement are used to model the data in the likelihood.

Similarly, in each bin and category, and in the diphoton fiducial region, an extended likelihood function is constructed from the $m_{\gamma\gamma}$ distribution of data events in the range $m_{\gamma\gamma} \in [105, 160]$ GeV, modeled using the signal and background parameterizations derived for each region. The likelihood used in the production mode and simplified template cross section measurements is the product of extended likelihood functions from each reconstruction category. For each differential cross section measurement, the likelihood is taken as the product of extended likelihood functions from each bin in the distribution.

Systematic uncertainties are incorporated into the likelihood function of each bin, category and region using a set of Gaussian or log-normal constraints on nuisance parameters. The full list and treatment of systematic uncertainties is discussed in Section 7.

7 Systematic uncertainties

Systematic uncertainties considered in this analysis can be grouped into three categories: (i) uncertainties in the signal and background modeling of the $m_{\gamma\gamma}$ spectrum, (ii) experimental uncertainties affecting the expected signal yields in each reconstruction category and differential bin, and in the diphoton fiducial region, and (iii) theoretical uncertainties in the signal yield modeling. These systematic uncertainties are discussed in the following sections.

The measurements based on event reconstruction categories incorporate the yield uncertainties and the $m_{\gamma\gamma}$ spectrum uncertainties directly into the likelihood function (described in Section 6.3), which is used to extract the signal strength or cross section. For the measurements of fiducial and differential cross sections, the likelihood function is constructed using only the uncertainties in the modeling of the $m_{\gamma\gamma}$ spectrum to extract the signal events, and yield uncertainties are incorporated at a later stage as part of a correction factor (introduced in Section 9.2) or part of the luminosity. Theoretical uncertainties are also evaluated differently as discussed in Sections 7.3 and 7.4.

7.1 Systematic uncertainties in the signal and background modeling of the $m_{\gamma\gamma}$ spectrum

The photon energy scale uncertainties shift the position of the signal peak by between $\pm 0.2\%$ and $\pm 0.4\%$, while the photon energy resolution uncertainties change the width of the signal peak by between $\pm 6\%$ and $\pm 15\%$, following Refs. [64, 82]. These uncertainties are implemented as independent sources of systematic uncertainty. Another uncertainty affecting the signal peak position is the uncertainty due to the knowledge of the Higgs boson mass of 0.24 GeV [83].

The uncertainty due to the background function choice is taken to be the spurious signal yield discussed in Section 6.2, and assumed to be uncorrelated between categories.

7.2 Experimental systematic uncertainties affecting the expected signal yields

The uncertainty in the combined 2015-2017 integrated luminosity is 2.0%. It is derived, following a methodology similar to that detailed in Ref. [84], from a preliminary calibration of the luminosity scale using x - y beam-separation scans.

Other sources of experimental uncertainties affecting the expected signal yields include: the efficiency of the diphoton trigger [12], the photon identification efficiencies [61], the photon isolation efficiencies, the photon energy scale and resolution [64, 82], the modeling of pile-up in the simulation, the jet energy scale and resolution [69, 85, 86], the efficiency of the jet vertex tagger, the efficiency of the b -tagging algorithm [87], the electron [75] and muon [76] reconstruction, identification and isolation efficiencies, the electron [64] and muon [76] energy and momentum scale and resolution, as well as the contribution to E_T^{miss} from charged-particle tracks that are not associated with high- p_T electrons, muons, jets, or photons [77]. Among these, the uncertainties with the largest variations in signal yields are the jet energy scale and resolution uncertainties (up to 24%) and photon isolation efficiency uncertainties (4-5%).

7.3 Theoretical modeling uncertainties for production mode and simplified template results

For the production mode and simplified template cross section measurements, the theoretical modeling uncertainties affecting the acceptance and efficiency of Higgs boson production processes include those due to:

- missing higher-order terms in the perturbative QCD calculations, estimated by varying the renormalization and factorization scales. For the gluon–gluon fusion process, nine additional uncertainty sources are included for the missing higher-order QCD corrections: four sources [9, 88–90] account for modeling uncertainties in the jet multiplicities; three sources parameterize modeling uncertainties in the Higgs boson p_T ; two sources [91, 92] account for the uncertainty in the acceptance of gluon–gluon fusion events in the VBF categories. The variations due to these uncertainties range from less than 1% to 27%.
- the choice of parton distribution functions and the value of α_S , estimated using the PDF4LHC15 recommendations [21]. Their effects are usually small.
- the modeling of the parton shower, underlying event, and hadronization, assessed by comparing the acceptance of simulated signal samples showered with Pythia to that of samples showered with Herwig. For the ggF process, the effects of the eigenvector tunes from the AZNLO set are merged to provide one additional uncertainty. The variations due to these uncertainties range from less than 1% to 18%.

Finally, in the categories targeting the $t\bar{t}H$ processes, the predicted ggF, VBF and VH yields are each assigned a conservative 100% uncertainty (correlated between categories), which is due to the theoretical uncertainty in the radiation of additional heavy-flavor jets in these Higgs boson production modes. This is supported by measurements using $H \rightarrow ZZ^* \rightarrow 4\ell$ [93], $t\bar{t}b\bar{b}$ [94], and Vb [95, 96] events, and is consistent

with the $N_{b\text{-jets}}$ measurement reported in Section 9.4. The impact of this uncertainty on the results is small, due to the high $t\bar{t}H$ signal purity in these categories.

The uncertainty sources of missing higher-order QCD effects and choice of parton distribution functions affect both the process cross sections and the event kinematic properties. The cross section measurements do not consider the effect on the cross section prediction, while the signal strength measurements take both effects into account. Additionally, the signal strength measurements consider the $H \rightarrow \gamma\gamma$ branching ratio uncertainty [50–54].

7.4 Theoretical modeling uncertainties for fiducial integrated and differential results

The correction factors used to unfold detector-level distributions to the particle level, described in Section 9.2, are impacted by uncertainties in the modeling of Higgs boson production. The uncertainty in the fiducial integrated and differential cross sections due to theoretical modeling is evaluated by taking the envelope of the following three sources:

- the uncertainty in the relative contributions of the different Higgs boson production modes, evaluated by varying them within the corresponding experimental bounds [97].
- the uncertainty due to a possible mismodeling of the Higgs boson transverse momentum and rapidity distributions, estimated by reweighting the reconstruction-level distributions of selected events in simulation to match those observed in data.
- the uncertainty in the modeling of the parton shower, underlying event, and hadronization, derived using the same method as described in Section 7.3.

In addition, the correction factor removes a small fraction of reconstructed $H \rightarrow ff\gamma$ Dalitz decays, where f refers to any fermion except the top quark. These events are not considered as signal and are removed as part of the correction factor. A conservative (100%) uncertainty on the modeling of this process in simulated events is assessed as part of the correction factor uncertainty, and amounts to about 0.4% of the measured cross section.

The impact of the modeling uncertainties on fiducial integrated and differential cross section results is small, as shown in Section 9.5.

8 Measurement of production mode cross sections and simplified template cross sections

8.1 Event categorization

Events that satisfy the inclusive diphoton selection are classified into 29 exclusive categories that are optimized for the production mode cross section and stage-1 simplified template cross section measurements, as indicated in Figure 1. The categorization proceeds from the production modes with smaller expected cross sections, to the production modes with larger expected cross sections, in the order described below. Jets are required to have $p_T > 30$ GeV, except for $t\bar{t}H$ -enriched categories which use jets with p_T greater than 25 GeV. Throughout this section, reconstruction-level leptons refer to electrons and muons, as taus are not considered in the event categorization.

8.1.1 $t\bar{t}H$ enriched categories

To target the $t\bar{t}H$ process, 7 analysis categories are defined. Exactly the same analysis categories are used in Ref. [6]. These categories are either from a ‘Lep’ region, where at least one top quark decays to a charged lepton that is reconstructed and identified, or from a ‘Had’ region, where both top quarks decay to hadrons, or where the leptons from the top quark decays are not reconstructed or identified.

The ‘Had’ region selects events with no leptons and at least three jets, of which at least one is b -tagged using the working point with an 77% efficiency. A boosted decision tree (BDT), $\text{BDT}_{t\bar{t}H\text{had}}$, is trained using signal from the $t\bar{t}H$ simulation and background from a data control region that has the same selection as the ‘Had’ region except at least one of the two photons fails either identification or isolation requirements. This BDT exploits a number of object-level variables: the transverse momentum p_T , the pseudorapidity η , the azimuthal angle ϕ , the energy E and the b -tagging decision of up to 6 leading jets, the magnitude and ϕ of missing transverse momentum, as well as the $p_T/m_{\gamma\gamma}$, η , and ϕ of each of the two photons.

In the ‘Lep’ region, events are required to contain at least one lepton and at least one b -tagged jet. Similar to the ‘Had’ region, a BDT, $\text{BDT}_{t\bar{t}H\text{lep}}$, is trained on the $t\bar{t}H$ signal using the object-level variables of the missing transverse momentum and the photons. The background training sample is a data control region that differs from the ‘Lep’ region by requiring exactly 0 b -tagged jet, at least one central jet, and at least one of the two photons failing either identification or isolation requirements. Additionally, this BDT uses the p_T , η , ϕ and E of up to four leading jets and two leading leptons.

The BDTs, trained using the XGBoost package [98], maximize the usage of event information and thus efficiently separate the $t\bar{t}H$ signal from major backgrounds, including $\gamma\gamma$, $t\bar{t}\gamma\gamma$, and the other Higgs production modes. Using several control samples in data and simulation, it is further checked that the BDTs do not artificially create a peak in the $m_{\gamma\gamma}$ spectrum, which would introduce a large spurious signal yield. Furthermore, to better exploit the BDT separation power, four (three) categories in the ‘Had’ (‘Lep’) region are defined using the BDT output. Events with low BDT output values do not enter these categories and are assigned to non- $t\bar{t}H$ categories as discussed in the next Section.

8.1.2 Non- $t\bar{t}H$ categories

The other reconstruction categories target the VH , VBF, and ggF production modes:⁴

- 5 categories are enriched in VH production with leptonic decays of the vector bosons:

The VH dilepton (“VH dilep”) category requires the presence of two same-flavor opposite-sign leptons with the invariant mass of the two leptons ($m_{\ell\ell}$) between 70 GeV and 110 GeV. In the two VH one-lepton categories, events are required to have exactly one electron or muon, and single-electron events are vetoed if the invariant mass of the selected electron and any of the two signal photons ($m_{e\gamma}$) is between 84 GeV and 94 GeV. The “VH lep High” (“VH lep Low”) category requires the p_T of the system of E_T^{miss} plus the lepton, $p_T^{\ell+E_T^{\text{miss}}}$, to be higher (lower) than 150 GeV. Additionally, an E_T^{miss} significance ($E_T^{\text{miss}}/\sqrt{\sum E_T}$) > 1.0 requirement is applied to the “VH lep Low” category. Among the two VH missing transverse momentum categories, the “VH MET Low”

⁴ Some of the non- $t\bar{t}H$ category names have changed slightly from Ref. [7], however the definition of those categories remains the same.

category requires $80 \text{ GeV} < E_T^{\text{miss}} < 150 \text{ GeV}$ and E_T^{miss} significance > 8 , while the “VH MET High” category requires either $E_T^{\text{miss}} > 150 \text{ GeV}$ and E_T^{miss} significance > 9 , or $E_T^{\text{miss}} > 250 \text{ GeV}$.

- 7 categories enhance the sensitivity to VH production with hadronic decays of the vector bosons and VBF production:

The “qqH BSM” category is defined by events with at least 2 jets and the transverse momentum of the leading jet ($p_{T,j1}$) greater than 200 GeV. In the two VH hadronic categories, events are required to have at least two jets with $60 < m_{jj} < 120 \text{ GeV}$, where m_{jj} is the dijet invariant mass. A BDT, BDT_{VH} , is trained to separate VH process from other processes. Using the BDT output as the discriminating variable, events are classified into the “VH had BDT tight” and “VH had BDT loose” categories.

In the four VBF categories, events are required to contain at least two jets, and the pseudorapidity separation between the two leading jets ($|\Delta\eta_{jj}|$) is required to be greater than 2. In addition, $|\eta_{\gamma\gamma} - 0.5(\eta_{j1} + \eta_{j2})|$ is required to be less than 5, where $\eta_{\gamma\gamma}$ denotes the pseudorapidity of the diphoton system and η_{j1} (η_{j2}) denotes the pseudorapidity of the leading (sub-leading) jet. Based on the transverse momentum p_T^{Hjj} of the vector sum of the momenta of the reconstructed Higgs boson and of the two leading jets, events are split into a $p_T^{Hjj} < 25 \text{ GeV}$ region and a $p_T^{Hjj} > 25 \text{ GeV}$ region. Another BDT, BDT_{VBF} , is trained to separate VBF process from other processes. Four exclusive categories are then defined with “tight” and “loose” requirements on the BDT classifier in the two p_T^{Hjj} regions: “VBF high- p_T^{Hjj} BDT tight”, “VBF high- p_T^{Hjj} BDT loose”, “VBF low- p_T^{Hjj} BDT tight”, “VBF low- p_T^{Hjj} BDT loose”. In these VH hadronic and VBF categories, except “VBF low- p_T^{Hjj} BDT tight”, more than half of the signal is expected to be from the ggF production.

- 10 categories measure the properties of events from ggF production:

The remaining events (mainly from ggF production) are separated into events with zero jets, exactly one-jet, or at least two jets. The zero-jet events are split into a “ggF 0J Cen” category where both photons are in the pseudorapidity region of $|\eta| < 0.95$, and a “ggF 0J Fwd” category where at least one photon in the pseudorapidity region of $|\eta| > 0.95$. The exclusive one-jet (“ggF 1J”) and inclusive two-jet (“ggF 2J”) events are further split into regions of diphoton transverse momentum: $p_T^{\gamma\gamma} \in [0, 60), [60, 120), [120, 200)$ and $> 200 \text{ GeV}$, denoted as “Low”, “Med”, “High” and “BSM”, respectively.

These categories were optimized using simulated events for the sensitivity to the production mode and simplified template cross sections. Their definitions remain the same as those in Ref. [7], except the “qqH BSM” category has been updated with a requirement of at least 2 jets, in order to better measure the corresponding simplified template cross section.

A summary of the definitions of all categories is provided in Table 3. Figure 4 shows the composition of signal events for each category in terms of different simplified template cross section regions, while Figure 5 shows the composition of signal events for each category in terms of different production modes. More information about the signal efficiencies times acceptance, composition of signal events, effective signal mass resolution, and number of signal and background events for each category can be found in Tables 9, 10 and 11 in the appendix.

Category label	Selection
ttH lep BDT1	$N_{\text{lep}} \geq 1, N_{b\text{-jet}} \geq 1, \text{BDT}_{\text{ttHlep}} > 0.987$
ttH lep BDT2	$N_{\text{lep}} \geq 1, N_{b\text{-jet}} \geq 1, 0.942 < \text{BDT}_{\text{ttHlep}} < 0.987$
ttH lep BDT3	$N_{\text{lep}} \geq 1, N_{b\text{-jet}} \geq 1, 0.705 < \text{BDT}_{\text{ttHlep}} < 0.942$
ttH had BDT1	$N_{\text{lep}} = 0, N_{\text{jets}} \geq 3, N_{b\text{-jet}} \geq 1, \text{BDT}_{\text{ttHhad}} > 0.996$
ttH had BDT2	$N_{\text{lep}} = 0, N_{\text{jets}} \geq 3, N_{b\text{-jet}} \geq 1, 0.991 < \text{BDT}_{\text{ttHhad}} < 0.996$
ttH had BDT3	$N_{\text{lep}} = 0, N_{\text{jets}} \geq 3, N_{b\text{-jet}} \geq 1, 0.971 < \text{BDT}_{\text{ttHhad}} < 0.991$
ttH had BDT4	$N_{\text{lep}} = 0, N_{\text{jets}} \geq 3, N_{b\text{-jet}} \geq 1, 0.911 < \text{BDT}_{\text{ttHhad}} < 0.971$
VH dilep	$N_{\text{lep}} \geq 2, 70 \text{ GeV} \leq m_{\ell\ell} \leq 110 \text{ GeV}$
VH lep High	$N_{\text{lep}} = 1, m_{e\gamma} - 89 \text{ GeV} > 5 \text{ GeV}, p_{\text{T}}^{\ell+E_{\text{T}}^{\text{miss}}} > 150 \text{ GeV}$
VH lep Low	$N_{\text{lep}} = 1, m_{e\gamma} - 89 \text{ GeV} > 5 \text{ GeV}, p_{\text{T}}^{\ell+E_{\text{T}}^{\text{miss}}} < 150 \text{ GeV}, E_{\text{T}}^{\text{miss}} \text{ significance} > 1$
VH MET High	$150 \text{ GeV} < E_{\text{T}}^{\text{miss}} < 250 \text{ GeV}, E_{\text{T}}^{\text{miss}} \text{ significance} > 9 \text{ or } E_{\text{T}}^{\text{miss}} > 250 \text{ GeV}$
VH MET Low	$80 \text{ GeV} < E_{\text{T}}^{\text{miss}} < 150 \text{ GeV}, E_{\text{T}}^{\text{miss}} \text{ significance} > 8$
qqH BSM	$N_{\text{jets}} \geq 2, p_{\text{T,j1}} > 200 \text{ GeV}$
VH had BDT tight	$60 \text{ GeV} < m_{\text{jj}} < 120 \text{ GeV}, \text{BDT}_{\text{VH}} > 0.78$
VH had BDT loose	$60 \text{ GeV} < m_{\text{jj}} < 120 \text{ GeV}, 0.35 < \text{BDT}_{\text{VH}} < 0.78$
VBF high- p_{T}^{Hjj} BDT tight	$ \Delta\eta_{jj} > 2, \eta_{\gamma\gamma} - 0.5(\eta_{j1} + \eta_{j2}) < 5, p_{\text{T}}^{Hjj} > 25 \text{ GeV}, \text{BDT}_{\text{VBF}}^{\text{high}} > 0.47$
VBF high- p_{T}^{Hjj} BDT loose	$ \Delta\eta_{jj} > 2, \eta_{\gamma\gamma} - 0.5(\eta_{j1} + \eta_{j2}) < 5, p_{\text{T}}^{Hjj} > 25 \text{ GeV}, -0.32 < \text{BDT}_{\text{VBF}}^{\text{high}} < 0.47$
VBF low- p_{T}^{Hjj} BDT tight	$ \Delta\eta_{jj} > 2, \eta_{\gamma\gamma} - 0.5(\eta_{j1} + \eta_{j2}) < 5, p_{\text{T}}^{Hjj} < 25 \text{ GeV}, \text{BDT}_{\text{VBF}}^{\text{low}} > 0.87$
VBF low- p_{T}^{Hjj} BDT loose	$ \Delta\eta_{jj} > 2, \eta_{\gamma\gamma} - 0.5(\eta_{j1} + \eta_{j2}) < 5, p_{\text{T}}^{Hjj} < 25 \text{ GeV}, 0.26 < \text{BDT}_{\text{VBF}}^{\text{low}} < 0.87$
ggF 2J BSM	$N_{\text{jets}} \geq 2, p_{\text{T}}^{\gamma\gamma} \geq 200 \text{ GeV}$
ggF 2J High	$N_{\text{jets}} \geq 2, p_{\text{T}}^{\gamma\gamma} \in [120, 200] \text{ GeV}$
ggF 2J Med	$N_{\text{jets}} \geq 2, p_{\text{T}}^{\gamma\gamma} \in [60, 120] \text{ GeV}$
ggF 2J Low	$N_{\text{jets}} \geq 2, p_{\text{T}}^{\gamma\gamma} \in [0, 60] \text{ GeV}$
ggF 1J BSM	$N_{\text{jets}} = 1, p_{\text{T}}^{\gamma\gamma} \geq 200 \text{ GeV}$
ggF 1J High	$N_{\text{jets}} = 1, p_{\text{T}}^{\gamma\gamma} \in [120, 200] \text{ GeV}$
ggF 1J Med	$N_{\text{jets}} = 1, p_{\text{T}}^{\gamma\gamma} \in [60, 120] \text{ GeV}$
ggF 1J Low	$N_{\text{jets}} = 1, p_{\text{T}}^{\gamma\gamma} \in [0, 60] \text{ GeV}$
ggF 0J Fwd	$N_{\text{jets}} = 0, \text{one photon with } \eta > 0.95$
ggF 0J Cen	$N_{\text{jets}} = 0, \text{two photons with } \eta \leq 0.95$

Table 3: Summary of the 29 event reconstruction categories for the measurement of production mode cross sections and simplified template cross sections. Each category targets a particle-level kinematic region that is reflected in the category label. Each event is assigned to the first category whose requirements are satisfied, using the descending order given in the table. As a result, the event populations of categories are mutually exclusive. Note that the categories are separated by horizontal lines based on the definitions of the stage-0 simplified template cross sections: top, VH leptonic, $qq' \rightarrow Hqq'$ (VBF + VH), and ggF. Though some of the non- $t\bar{t}H$ category names have changed, the definition of those categories is the same as in Ref. [7]. N_{lep} denotes the number of selected electrons and muons, N_{jets} the number of selected jets, and $N_{b\text{-jet}}$ the number of b -tagged jets. Other variables are defined in the text.

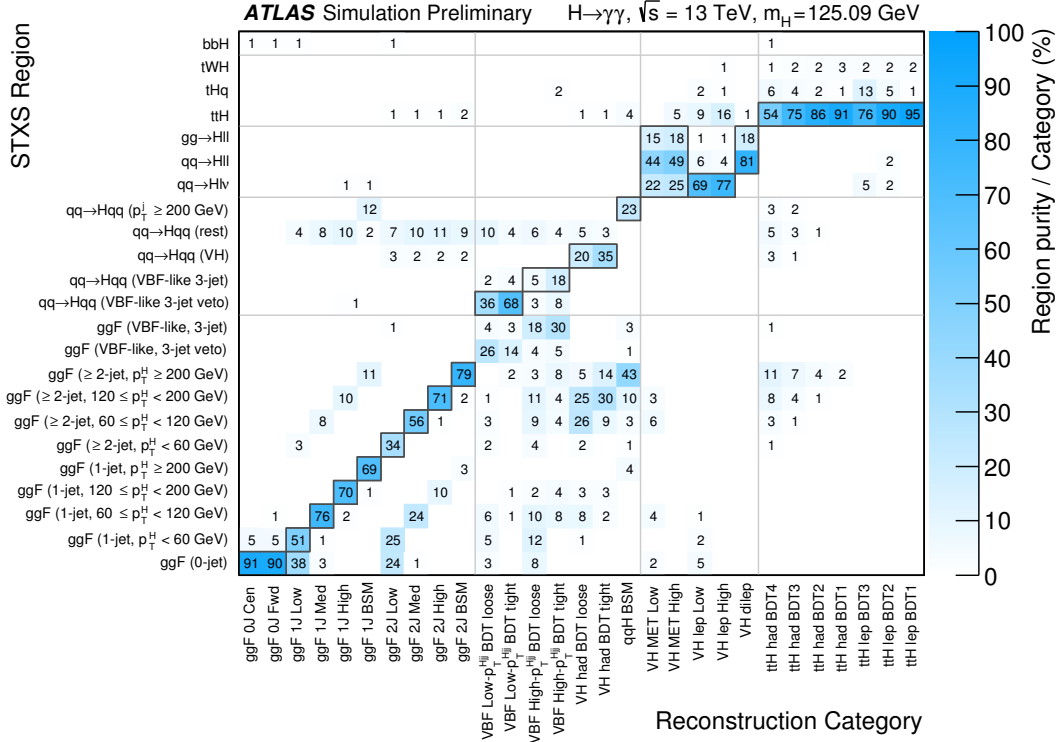


Figure 4: The expected composition of signal events, as classified by the particle-level regions (rows) of the stage-1 simplified template cross sections (STXS), in each reconstruction category (columns). Some stage-1 regions are merged in cases where the data set lacks the sensitivity to resolve them. For each reconstruction category, the target particle-level categories are indicated with a box. The gray horizontal and vertical lines delimit stage-0 STXS regions and their corresponding reconstruction categories. Numbers in each column add up to 100%. Entries smaller than 1% are suppressed.

8.2 Production mode measurements

The global signal strength, production mode cross sections and simplified template cross sections are extracted using simultaneous fits to the diphoton invariant mass distribution in the 29 categories, with the extended likelihood functions described in Section 6.3.

8.2.1 Observed Data

Figure 6 and Figure 7 show the weighted diphoton invariant mass distributions observed in 79.8 fb^{-1} of 13 TeV data using all analysis categories. Events are weighted by $\ln(1 + S_{90}/B_{90})$, where S_{90} (B_{90}) for each category is the expected signal (background) in the smallest $m_{\gamma\gamma}$ window containing 90% of the expected signal. In Figure 6, the signal is the sum of all Higgs production modes. In Figure 7 (a) - (d), the signal is ggF, VBF, VH , and top-associated production, respectively, while the other Higgs boson production modes are included in the background. In both figures, the solid red curve shows the fitted signal-plus-background model with the Higgs boson mass constrained to 125.09 ± 0.24 GeV. This constraint is consistent with the observed mass peak position. The fit is performed in all analysis categories for the global signal strength, assuming the relative ratios of different production modes are as predicted by the

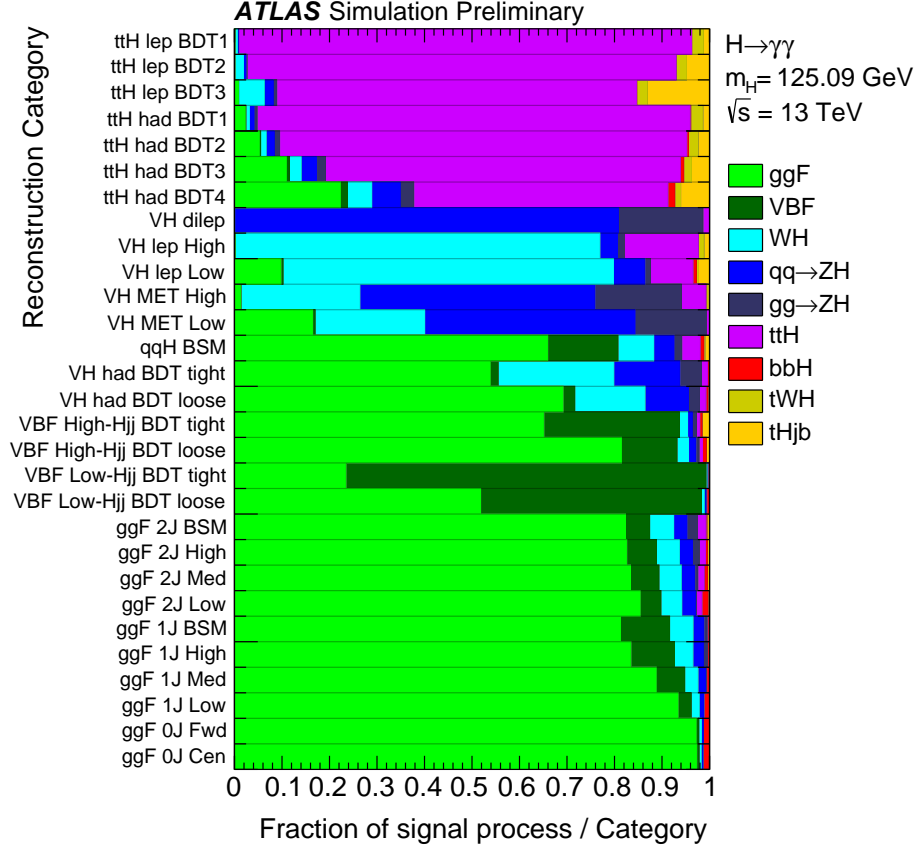


Figure 5: The expected composition of signal events, based on production mode, of each reconstruction category.

SM. The non-resonant background component is shown with the dotted blue curve. In Figure 7, the total background component is shown with the dashed green curve. Both the signal-plus-background and background-only curves shown here are obtained from the weighted sum of the individual curves in each analysis category.

8.2.2 Production mode cross sections

A global signal strength μ is measured for the inclusive Higgs boson production, assuming the ratios of different production modes are the same as in the SM prediction within the assigned theoretical systematic uncertainties. μ is found to be

$$\mu = 1.06^{+0.14}_{-0.12} = 1.06 \pm 0.08 \text{ (stat.) }^{+0.08}_{-0.07} \text{ (exp.) }^{+0.07}_{-0.06} \text{ (theo.)} ,$$

which is consistent with the SM expectation ($\mu = 1$). The global signal strength measurement is dominated by the systematic uncertainty, for which the experimental uncertainty and theoretical uncertainty have similar importance.

The production mode cross sections are evaluated in a region with Higgs-boson rapidity $|y_H| < 2.5$. σ_{top} , denoted as the sum of the $t\bar{t}H$, tHq , and tHW production mode cross sections, is fitted under the assumption that their relative ratios are as predicted by the SM. Similarly, the VH production mode cross

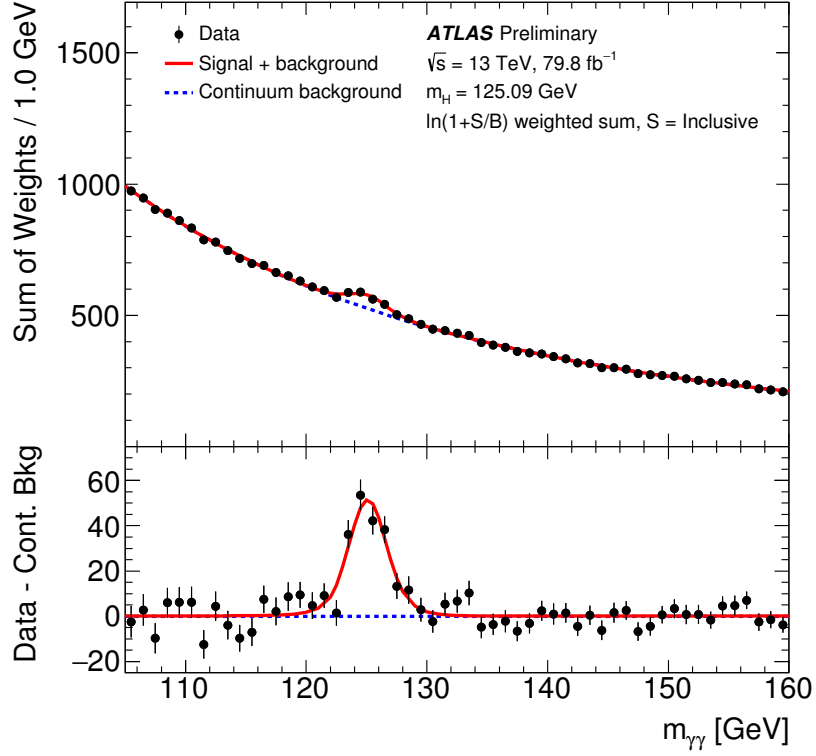


Figure 6: Weighted diphoton invariant mass spectrum in all the analysis categories observed in 79.8 fb^{-1} of 13 TeV data. Events are weighted by $\ln(1 + S_{90}/B_{90})$, where S_{90} (B_{90}) for each category is the expected signal (background) in the smallest $m_{\gamma\gamma}$ window containing 90% of the expected signal. The signal is the sum of all Higgs production modes. The error bars represent 68% confidence intervals of the weighted sums. The solid red curve shows the fitted signal-plus-background model with the Higgs boson mass constrained to $125.09 \pm 0.24 \text{ GeV}$. The fit is done in all the analysis categories for the global signal strength, assuming the relative ratios of different production modes are as predicted by the SM. The non-resonant background component of the fitted signal-plus-background model is shown with the dotted blue curve. Both the signal-plus-background and background-only curves shown here are obtained from the weighted sum of the individual curves in each analysis category. The lower panel shows the residuals between the data and the non-resonant background component.

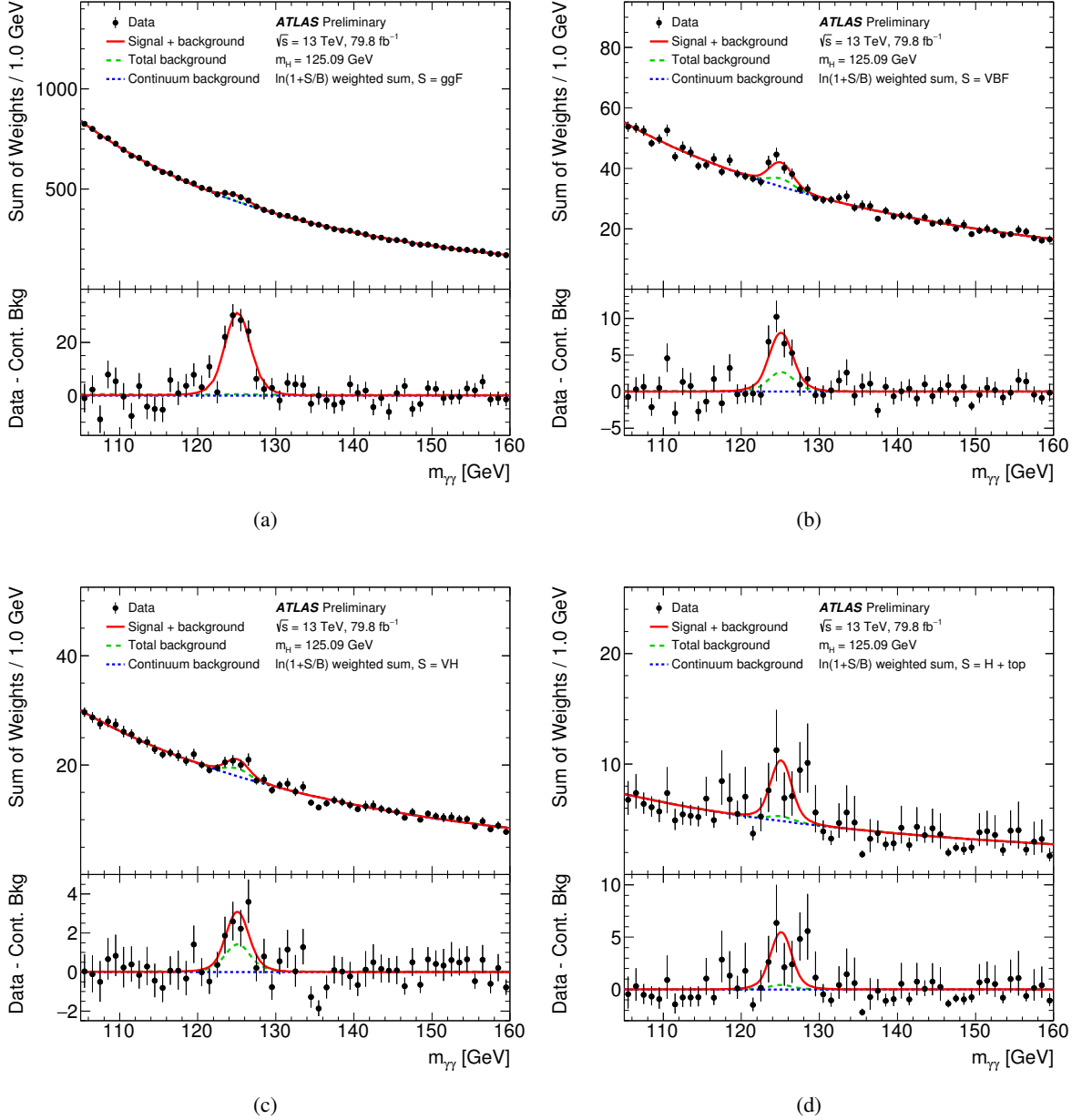


Figure 7: Weighted diphoton invariant mass spectrum in all the analysis categories observed in 79.8 fb^{-1} of 13 TeV data. Events are weighted by $\ln(1 + S_{90}/B_{90})$, where S_{90} (B_{90}) for each category is the expected signal (background) in the smallest $m_{\gamma\gamma}$ window containing 90% of the expected signal. The signal is (a) ggF, (b) VBF, (c) VH , and (d) top-associated production, respectively, while the other Higgs boson production modes are included in the background. The error bars represent 68% confidence intervals of the weighted sums. The solid red curve shows the fitted signal-plus-background model with the Higgs boson mass constrained to $125.09 \pm 0.24 \text{ GeV}$. The fit is done in all the analysis categories for the global signal strength, assuming the relative ratios of different production modes are as predicted by the SM. The non-resonant and total background components of the fitted signal-plus-background model are shown with the dotted blue curve and dashed green curve. Both the signal-plus-background and background-only curves shown here are obtained from the weighted sum of the individual curves in each analysis category. The lower panel shows the residuals between the data and the non-resonant background component.

Process ($ y_H < 2.5$)	Result [fb]	Uncertainty [fb]				SM prediction [fb]
		Total	(Stat.	Exp.	Theo.)	
ggF	98	$^{+15}_{-14}$	(± 11	$^{+9}_{-8}$	$^{+4}_{-3}$	102^{+5}_{-7}
VBF	11.2	$^{+3.4}_{-3.0}$	($^{+2.6}_{-2.4}$	$^{+1.3}_{-1.2}$	$^{+1.9}_{-1.1}$	8.0 ± 0.2
VH	4.9	$^{+2.7}_{-2.5}$	($^{+2.4}_{-2.2}$	$^{+1.0}_{-0.9}$	$^{+0.6}_{-0.5}$	4.5 ± 0.2
Top	1.5	$^{+0.6}_{-0.5}$	($^{+0.5}_{-0.4}$	± 0.2	$^{+0.2}_{-0.1}$	1.3 ± 0.1

Table 4: Best-fit values and uncertainties of the production mode cross sections (for $|y_H| < 2.5$) times the Higgs to diphoton branching ratio. The SM predictions [9] are shown for each production process. The central values and uncertainties are rounded.

section (including both the hadronic and leptonic decays of the vector boson) value is fitted using the SM prediction of the relative ratios of the WH , $q\bar{q}' \rightarrow ZH$, and $gg \rightarrow ZH$ production mode cross sections. The $b\bar{b}H$ contributions are merged with ggF, assuming the relative contributions are as predicted by the SM. The above processes are merged without considering the theoretical uncertainties on their relative ratios, while the impact of such uncertainties is found to be small.

Table 4 and Figure 8 present the measured production mode cross sections, multiplied by the branching ratio of the Higgs boson decay to two photons. These measurements are in agreement with the SM predictions. Observed (expected) correlations between the ggF, VBF, VH and top-associated production mode measurements are shown in Figure 9 (Figure 15 in the appendix). These correlations are found to be small.

Despite sharing the same methodology and data set, the measurement of the $t\bar{t}H$ production mode in this note ($(\sigma \times B)/(\sigma \times B)_{SM} = 1.12^{+0.43}_{-0.37}$) differs from that in Ref. [6] ($\sigma/\sigma_{SM} = 1.39^{+0.48}_{-0.42}$). This is due to different treatment of the other production modes, which were fixed to the SM prediction in Ref. [6] and are fit to data here, and to different effects of the systematic uncertainties derived from the fit of additional categories. Additionally, unlike σ_{top} used in this note, the $t\bar{t}H$ production mode cross section $\sigma_{t\bar{t}H}$ in Ref. [6] is a total cross section without the restriction of $|y_H| < 2.5$, and is not merged with the tHq and tHW production mode cross sections.

8.2.3 Simplified template cross sections

Because the current data set is not yet sensitive to all of the 31 regions in the “stage-1” scheme of the simplified template cross section framework, the stage-1 regions are merged to obtain 9 phase space regions as shown in Figure 1 and Table 1. This scheme has been chosen to reduce strong anti-correlations between the measured cross sections and to keep measurements near or below 100% total uncertainty. The “gluon–gluon fusion $p_T^H > 200$ GeV” and “VBF $p_T^j > 200$ GeV” regions in stage-1 are sensitive to BSM Higgs boson production. Due to their large anti-correlation, only the sum of these two cross sections is quoted, while their difference is profiled in the likelihood fit.

Table 5 and Figure 10 report the simplified template cross sections, multiplied by the branching ratio of the Higgs boson decay to two photons, in the 9 measured regions. In all regions, the measurements are consistent with the SM predictions. Observed (expected) correlations between the measured simplified

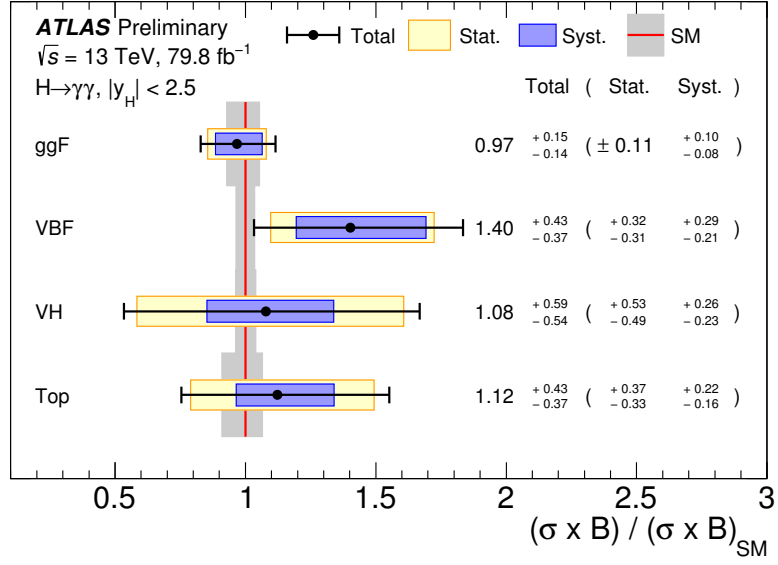


Figure 8: Summary plot of the measured production mode cross sections (for $|y_H| < 2.5$) times the Higgs to diphoton branching ratio. For illustration purposes the central values and uncertainties have been divided by their SM expectations. The uncertainties in the predicted SM cross sections are shown in gray bands in the plot.

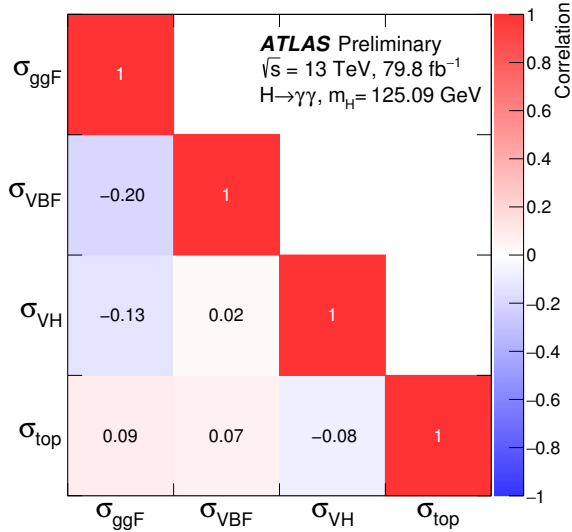


Figure 9: Observed correlations between the ggF, VBF, VH and top-associated production mode measurements, including both the statistical and systematic uncertainties.

Measurement region ($ y_H < 2.5$)	Result [fb]	Uncertainty [fb]				SM prediction [fb]
		Total	(Stat. Exp. Theo.)			
ggF, 0 jet	58	$^{+15}_{-14}$	(± 11 $^{+10}_{-8}$ $^{+2}_{-1}$)			63 \pm 5
ggF, 1 jet, $p_T^H < 60$ GeV	18	$^{+10}_{-9}$	(± 8 $^{+6}_{-5}$ $^{+1}_{-1}$)			15 \pm 2
ggF, 1 jet, $60 \leq p_T^H < 120$ GeV	9	± 5	(± 4 $^{+3}_{-2}$ $^{+1}_{-0}$)			10 \pm 2
ggF, 1 jet, $120 \leq p_T^H < 200$ GeV	2.6	$^{+1.5}_{-1.3}$	(± 1.2 $^{+0.8}_{-0.6}$ $^{+0.3}_{-0.1}$)			1.7 \pm 0.3
ggF, ≥ 2 jet	7	± 6	(± 5 $^{+3}_{-2}$ ± 2)			11 \pm 2
$qq \rightarrow Hqq$, $p_T^j < 200$ GeV	15	$^{+5}_{-4}$	(± 4 ± 2 ± 2)			10 \pm 0.5
ggF + $qq \rightarrow Hqq$, BSM-like	1.4	± 0.9	(± 0.8 ± 0.4 ± 0.2)			1.8 \pm 0.4
VH, leptonic	2.0	$^{+1.1}_{-1.0}$	($^{+1.0}_{-0.9}$ ± 0.4 ± 0.1)			1.4 \pm 0.1
Top	1.5	$^{+0.6}_{-0.5}$	(± 0.5 ± 0.2 ± 0.2)			1.3 \pm 0.1

Table 5: Best-fit values and uncertainties of the simplified template cross sections times the Higgs to diphoton branching ratio. The SM predictions [9] are shown for each region. The central values and uncertainties are rounded.

template cross section regions are shown in Figure 11 (Figure 16 in the appendix). These correlations are found to be small, except the correlation between the “ggF, 0 jet” and “ggF, 1 jet, $p_T^H < 60$ GeV” regions and the correlation between the “ggF, ≥ 2 jet” and “ $qq \rightarrow Hqq$, $p_T^j < 200$ GeV” regions, which are caused by their overlap in certain event reconstruction categories as shown in Figure 4.

The residual theoretical uncertainties in the nine measured regions are small compared to the experimental and statistical uncertainties. The theoretical uncertainties on the cross section of the nine phase space regions are given for the SM prediction in Table 5, and the remaining theoretical uncertainties impacting the measurements are acceptable for the current experimental precision.

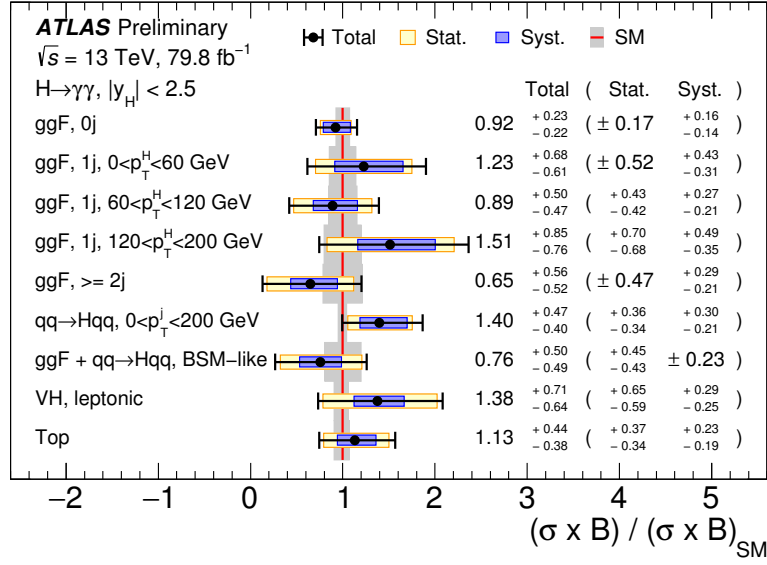


Figure 10: Summary plot of the measured simplified template cross sections times the Higgs to diphoton branching ratio. For illustration purposes the central values and uncertainties have been divided by their SM expectations. The uncertainties in the predicted SM cross sections are shown in gray in the plot. The definition of the measured regions can be found in Figure 1 and Table 1.

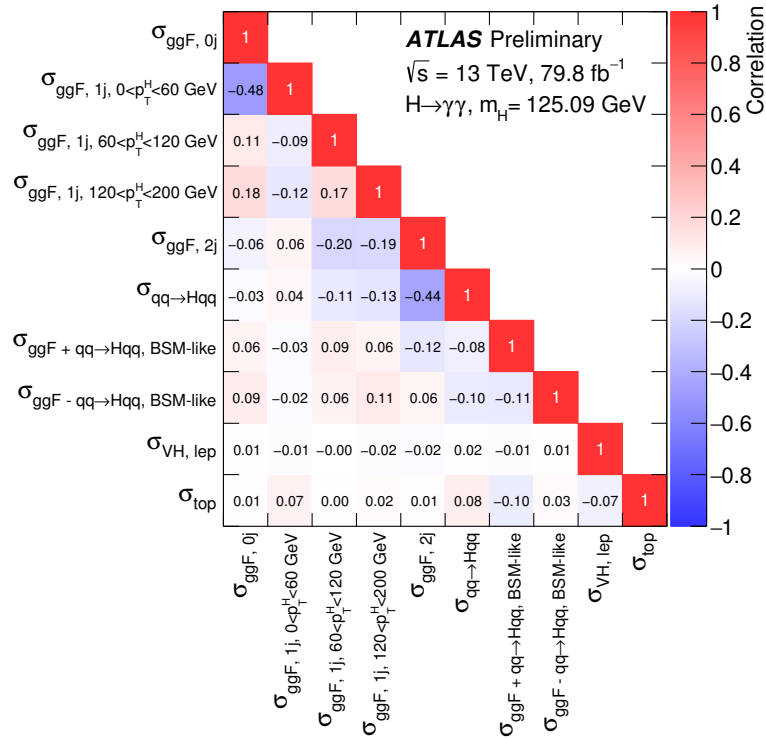


Figure 11: Observed correlations between the measured simplified template cross section regions, including both the statistical and systematic uncertainties.

9 Measurement of fiducial and differential cross sections

Fiducial integrated and differential cross section measurements provide a complementary method of studying the Higgs boson in addition to the production mode and coupling measurements presented in the previous section. Fiducial differential cross sections offer minimal model dependence, and variables are chosen for differential measurement that probe key properties of the Higgs boson. Fiducial and differential measurements are corrected for detector effects, and the results are reported at the particle level. In order to minimize extrapolation uncertainties, the particle-level fiducial selection is defined to resemble the ATLAS detector acceptance.

9.1 Particle-level fiducial definition of the Higgs boson diphoton cross sections

Measurements of the fiducial and differential Higgs boson production cross section are reported at the particle level. For the definition of the fiducial volume, only stable particles defined as having a lifetime of $\tau > 10$ ps are considered. Furthermore, particle-level photons, electrons and muons are defined as not having originated from a hadron.

To define the diphoton fiducial region, the two highest p_T photons satisfying $|\eta| < 2.37$ and outside the region $1.37 < |\eta| < 1.52$ are considered. The leading (subleading) photon must satisfy $p_T/m_{\gamma\gamma} > 0.35$ (0.25). Both photons must satisfy a particle-level isolation requirement constructed using $p_T^{\text{iso},0.2}$, the vector sum of transverse momenta of all charged stable particles with $p_T > 1$ GeV inside a cone $\Delta R = 0.2$ around the photon. The photons must satisfy $p_T^{\text{iso},0.2} < 0.05 p_T^\gamma$.

A lepton (e or μ) veto is used in the measurement of $N_{b\text{-jets}}$ to suppress Higgs boson production in association with top quarks. Particle-level electrons are required to satisfy $p_T > 10$ GeV and $|\eta| < 2.47$; electrons with $1.37 < |\eta| < 1.52$ are excluded. Electrons are rejected if they are within a cone of $\Delta R = 0.4$ around one of the two photons. Muons must satisfy $p_T > 10$ GeV and $|\eta| < 2.7$.

Jets are constructed from all particles, excluding muons and neutrinos, using the anti- k_t algorithm with radius parameter 0.4. Particle-level jets must have $p_T > 30$ GeV, $|y| < 4.4$, and must be separated from photons with $p_T > 25$ GeV ($\Delta R > 0.4$) and electrons with $p_T > 10$ GeV ($\Delta R > 0.2$). A jet is considered central (abbreviated “Cen”) if it has a rapidity $|y| < 2.5$. Jets are considered to originate from a b -hadron if there is a b -hadron with $p_T > 5$ GeV within a cone of radius $\Delta R = 0.4$ around the jet, and if the jet is central (to match the reconstruction-level definition).

9.2 Fiducial and differential cross section definitions

The diphoton fiducial region is used for the inclusive cross section measurement and the differential cross section measurements in bins of $p_T^{\gamma\gamma}$, $|y_{\gamma\gamma}|$, and p_T^{J1} . At the particle level, this region requires at least two photons satisfying the kinematic requirements described in the previous section. The differential measurement of central b -jets produced in association with the Higgs boson requires in addition at least one central jet and no particle-level electrons or muons. The particle-level definitions for the diphoton fiducial and differential cross section measurements are summarized in Table 6.

Although the fiducial region of the $N_{b\text{-jets}}$ measurement has a lepton veto meant to suppress $t\bar{t}H$, the measurement of $N_{b\text{-jets}}$ treats all Higgs production modes inclusively. Thus, the residual $t\bar{t}H$ is considered as signal alongside all other Higgs boson production modes. $t\bar{t}H$ accounts for about 18% of the expected

Objects	Definition
Photons	$ \eta < 1.37$ or $1.52 < \eta < 2.37$, $p_T^{\text{iso},0.2}/p_T^\gamma < 0.05$
Jets	anti- k_t , $R = 0.4$, $p_T > 30 \text{ GeV}$, $ y < 4.4$
– Central jets	$ y < 2.5$
– b -jets	$ y < 2.5$, $\Delta R(\text{jet}, b\text{-hadron}) < 0.4$ for b -hadrons with $p_T > 5 \text{ GeV}$
Leptons, $\ell = e$ or μ	electrons: $p_T > 10 \text{ GeV}$, $ \eta < 2.47$ (excluding $1.37 < \eta < 1.52$) muons: $p_T > 10 \text{ GeV}$, $ \eta < 2.7$
Fiducial region	Definition
Diphoton fiducial	$N_\gamma \geq 2$, $p_T^{\gamma_1} > 0.35 \cdot m_{\gamma\gamma}$, $p_T^{\gamma_2} > 0.25 \cdot m_{\gamma\gamma}$
$N_{b\text{-jets}}$ measurement	Diphoton fiducial, $N_{\text{jets}}^{\text{Cen}} \geq 1$, $N_{\text{leptons}} = 0$

Table 6: Definition of the particle-level objects and the fiducial measurement regions. The photon isolation $p_T^{\text{iso},0.2}$ is defined analogously to the reconstructed-level track isolation as the transverse momentum of the system of charged particles within $\Delta R < 0.2$ of the photon.

Higgs events in the $N_{b\text{-jets}}=1$ bin of the distribution, and 63% of the signal in the $N_{b\text{-jets}}\geq 2$ bin. Thus, Higgs boson production in association with heavy-flavor decays is probed primarily via the $N_{b\text{-jets}}=1$ bin.

The cross section measurement is performed in two steps: first, the number of signal events in data is extracted in each bin or region using a fit to the diphoton invariant mass spectrum as described in Section 6. In the second step, the reconstruction-level data signal yields are unfolded to the particle level using a bin-by-bin correction factor. The unfolded quantity is divided by the integrated luminosity, and the bin width in the case of a differential measurement, to obtain the fiducial (differential) cross section.

The cross section σ_i of a fiducial region i , and the fiducial differential cross section $d\sigma_i/dx$ in a bin i of variable x , are given by

$$\sigma_i = \frac{N_i^{\text{sig}}}{c_i \mathcal{L}_{\text{int}}} \quad \text{and} \quad \frac{d\sigma_i}{dx} = \frac{N_i^{\text{sig}}}{c_i \Delta x_i \mathcal{L}_{\text{int}}},$$

where N_i^{sig} is the signal yield extracted from data, c_i is a correction factor for detector efficiency and resolution effects, \mathcal{L}_{int} is the integrated luminosity of the data set, Δx_i is the differential distribution bin width. The correction factors used to unfold the data from reconstruction level to particle level are determined from the simulated samples discussed in Section 4. This unfolding method was determined to introduce minimal bias, performing as well as other unfolding methods with the given statistical limits of this measurement. In the diphoton fiducial region the correction factor is 0.73 ± 0.04 . Correction factors in the differential distributions typically range from 0.7 to 0.8, with the exception of certain bins in the $p_T^{\gamma_1}$ distribution, where migrations between bins can be significant, and bins in the $N_{b\text{-jets}}$ distribution, due to the low efficiency of the chosen b -tagging working point. Generally, photon identification efficiencies have the largest impact on the correction factors.

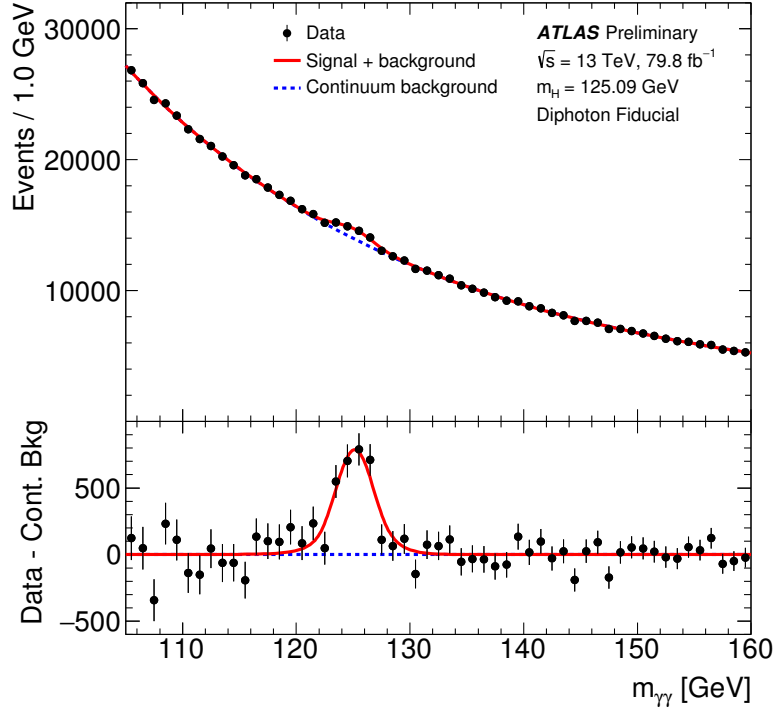


Figure 12: The diphoton invariant mass spectrum of events in the diphoton fiducial region. The solid red curve shows the fitted signal-plus-background model when the Higgs boson mass is constrained to 125.09 ± 0.24 GeV. The background component of the fitted signal-plus-background model is shown with the dotted blue curve. The bottom plot shows the residuals between the data and the background component of the fitted model.

9.3 Measurement of the inclusive fiducial cross section

The measured inclusive fiducial cross section is compared to a Standard Model prediction referenced in the text as the default MC prediction. This prediction includes a ggF component modeled using POWHEG NNLOPS and normalized to the $N^3\text{LO(QCD)+NLO(EW)}$ prediction of Refs. [9, 21, 32–35] and the diphoton decay branching ratio. The particle-level VBF, VH , top and $b\bar{b}H$ contributions (collectively called XH) are taken from the simulated samples and normalized using the cross section predictions described in Section 4.

Figure 12 reports the diphoton invariant mass spectrum of events in the diphoton fiducial region. The inclusive fiducial cross section times the Higgs to diphoton branching ratio is measured to be

$$\sigma_{\text{fid}} = 60.4 \pm 6.1 \text{ (stat.)} \pm 6.0 \text{ (exp.)} \pm 0.3 \text{ (theo.) fb},$$

which is within one standard deviation of the default SM prediction of 63.5 ± 3.3 fb.

9.4 Measurements of differential cross sections

Figure 13 reports the unfolded differential cross section $pp \rightarrow H \rightarrow \gamma\gamma$ as a function of $p_T^{\gamma\gamma}$, the diphoton transverse momentum; $|\eta_{\gamma\gamma}|$, the diphoton rapidity; $p_T^{j_1}$, the transverse momentum of the leading jet; and

$N_{b\text{-jets}}$, the number of b -jets in a fiducial region described in Table 6. In the differential measurement of $p_T^{j_1}$, the leading jet is defined at both particle and reconstruction level as the highest transverse-momentum jet satisfying the requirements listed in Table 6. The first bin of the $p_T^{j_1}$ distribution represents events that do not contain a jet with $p_T > 30$ GeV. Also, the first bin of the $N_{b\text{-jets}}$ distribution is the measured cross section of events with at least one central jet ($p_T > 30$ GeV) and no b -jets. The expected contribution of XH originating from $t\bar{t}H$ is depicted in the plot of $N_{b\text{-jets}}$ in order to highlight its contribution to the high b -jet multiplicity bins.

The unfolded differential distributions are compared to state-of-the-art theory predictions of gluon fusion production. Contributions from the other production modes are modeled using the XH simulated samples described in Section 9.3 and added to each gluon-fusion prediction before comparing to data. All data distributions are compared to:

- the default MC prediction (POWHEG NNLOPS normalized with the N³LO in QCD and NLO EW cross section) introduced in Section 9.3.

Additionally, the $p_T^{\gamma\gamma}$ distribution is compared to:

- NNLOJET+SCET [99], which provides predictions using a N³LL resummation matched to an NNLO fixed-order calculation in the heavy top limit. Additional corrections are applied for the fiducial selections of the analysis and are obtained from the default MC sample (POWHEG NNLOPS). The prediction is corrected to account for the efficiency of the particle-level photon isolation [7].

The $|y_{\gamma\gamma}|$ distribution is compared to:

- SCETLIB+MCFM8, which provides predictions for $|y_{\gamma\gamma}|$ at NNLO+NNLL' $_{\varphi}$ accuracy, derived by applying a resummation of the virtual corrections to the gluon form factor [100, 101].⁵ The underlying NNLO predictions are obtained using MCFM8 with zero-jettiness subtractions [102, 103]. The prediction is corrected for the particle-level photon isolation efficiency.

The $p_T^{j_1}$ distribution is compared to:

- The parton-level NNLOJET prediction of Refs. [104, 105], a fixed-order NNLO prediction in QCD for inclusive $H + 1$ -jet production. The NNLOJET prediction is compared to data in the phase space with at least 1 jet.
- SCETLIB(STWZ) [89, 101], which provides predictions for $p_T^{j_1}$ at NNLL'+NNLO₀ accuracy are derived applying a resummation in $p_T^{j_1}$.

Both the NNLOJET and SCETLIB predictions for $p_T^{j_1}$ are corrected for the particle-level photon isolation efficiency.

Theory estimates of the $N_{b\text{-jets}}$ distribution have poorly-understood uncertainties, and therefore the uncertainty band is omitted from the prediction in the comparison to data. All of these predictions are compatible with the measured differential distributions within the statistical limit.

⁵ The subscript φ refers to the fact that the applied resummation is to the gluon form factor.

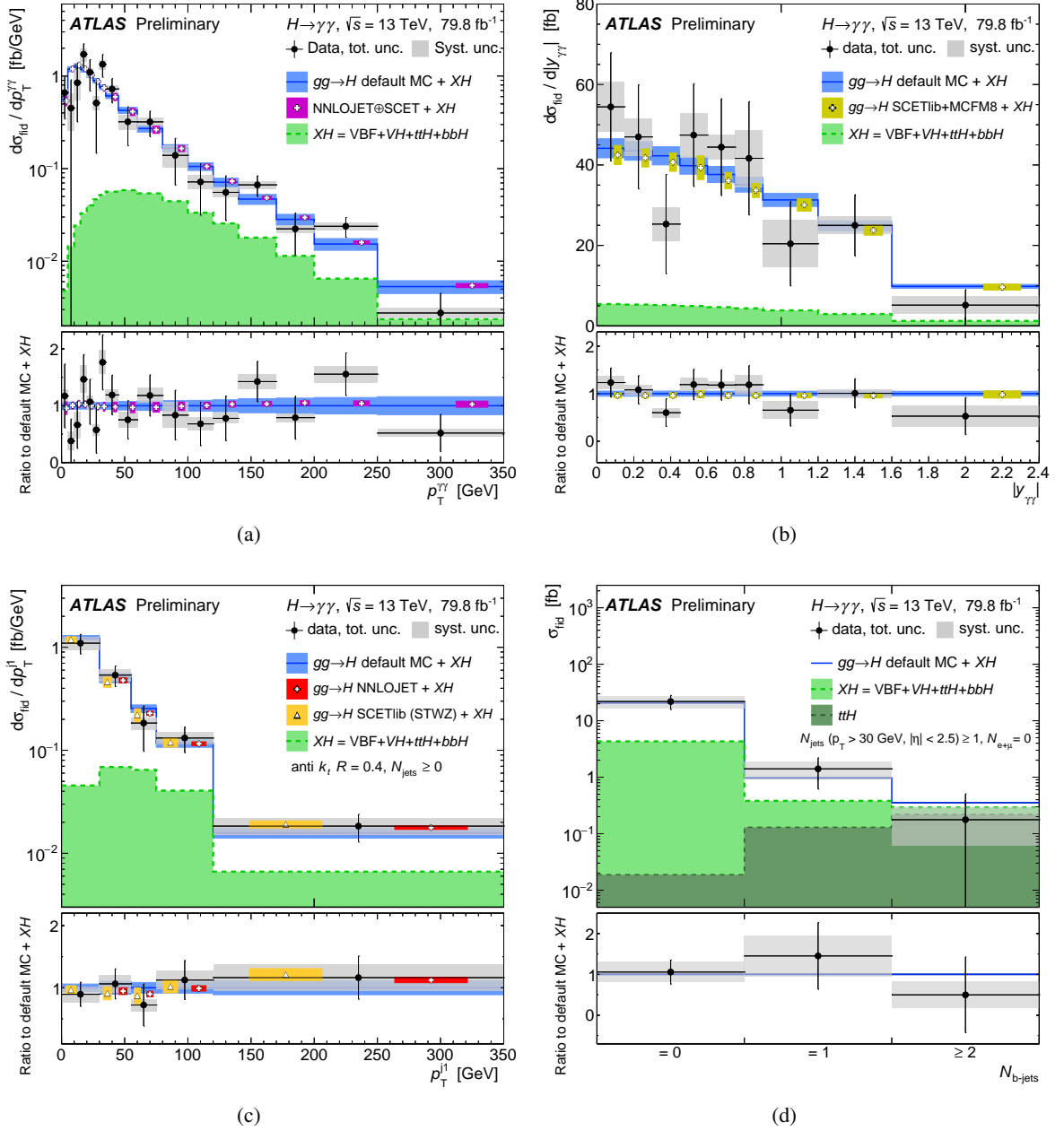


Figure 13: The fiducial differential cross sections measured as a function of (a) $p_T^{\gamma\gamma}$, (b) $|y_{\gamma\gamma}|$, (c) p_T^{j1} , and (d) $N_{b\text{-jets}}$. The $N_{b\text{-jets}}$ distribution is measured in a fiducial phase space requiring at least one central jet ($p_T > 30$ GeV, $|y| < 2.5$) and no electrons or muons. All differential measurements are compared to the default MC prediction, with gluon fusion modeled using POWHEG NNLOPS and other Higgs production processes XH using the predictions described in Section 4. In addition, the $p_T^{\gamma\gamma}$ distribution is compared to (XH plus) the gluon-fusion prediction NNLOJET+SCET; the $|y_{\gamma\gamma}|$ distribution is compared to SCETLIB+MCFM8; and the p_T^{j1} distribution is compared to NNLOJET and SCETLIB(STWZ), all described in Section 9.4. The theoretical uncertainty of the $N_{b\text{-jets}}$ prediction is not well understood, and is therefore omitted.

Source	Uncertainty (%)
Fit (stat.)	10
Fit (syst.)	8.3
Photon energy scale & resolution	4.0
Background modeling (spurious signal)	7.3
Correction factor	5.2
Photon isolation efficiency	4.6
Pileup	1.9
Photon ID efficiency	1.3
Trigger efficiency	0.7
Dalitz Decays	0.4
Theoretical modeling	+0.3 -0.4
Diphoton vertex selection	0.1
Photon energy scale & resolution	0.1
Luminosity	2.0
Total	14

Table 7: The breakdown of uncertainties on the inclusive diphoton fiducial cross section measurement. The fit uncertainties relate to the extraction of the number of signal events using the diphoton invariant mass spectrum. The remaining uncertainties are associated with unfolding, including the correction factor and luminosity.

9.5 Impact of systematic uncertainties on results

Table 7 reports the main systematic uncertainties for the cross section measurements in the diphoton fiducial region. The systematic uncertainties in each bin of the $p_T^{\gamma\gamma}$ and $N_{b\text{-jets}}$ distributions are reported in Figure 14; the uncertainties of the $|y_{\gamma\gamma}|$ and p_T^{j1} distributions are reported in Figure 17 in the appendix. The fiducial and differential measurements are dominated by statistical uncertainties. Among the systematic uncertainties, those associated to the signal extraction (background modeling, photon energy scale and resolution) are typically the largest.

Other experimental uncertainties contribute via their impact on the correction factor, also shown in Figures 14 and 17. For the inclusive fiducial cross section and the differential $p_T^{\gamma\gamma}$ and $|y_{\gamma\gamma}|$ measurements, the photon isolation efficiency, modeling of pile-up in simulation, and photon identification efficiency uncertainties contribute the most to the correction factor uncertainty. For the measurement of $N_{b\text{-jets}}$, the dominant correction factor uncertainties include the isolation efficiency, b -tagging efficiency (flavor tagging), and jet energy scale and resolution. For the differential p_T^{j1} measurement, the jet energy scale and resolution, photon isolation efficiency, and the efficiency of the jet vertex tagger are the main correction factor uncertainties.

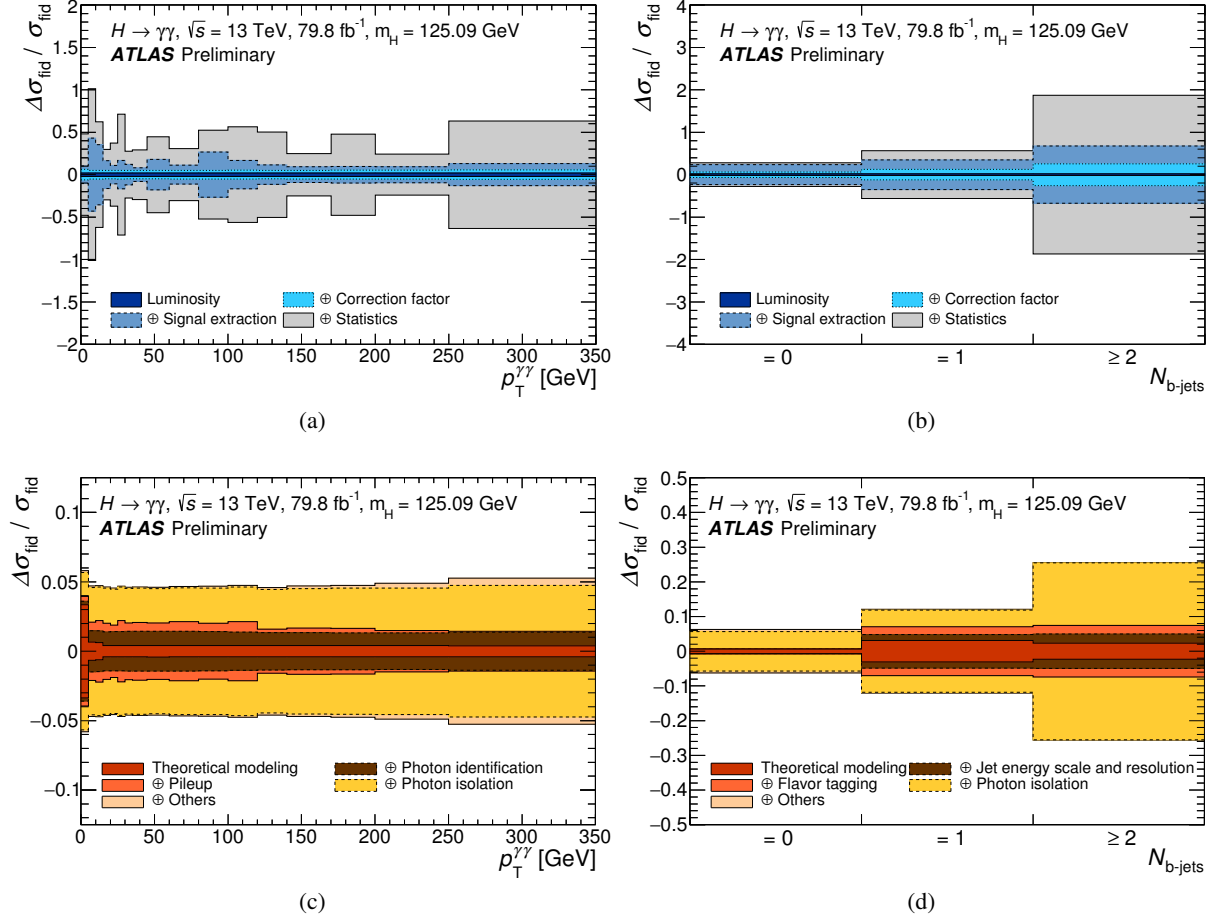


Figure 14: The systematic uncertainties, relative to the differential cross sections measured in data, in each bin of the (a) the $p_T^{\gamma\gamma}$ and (b) the $N_{b\text{-jets}}$ differential distributions, sequentially summed in quadrature. The systematic uncertainty is composed of luminosity, signal extraction and correction factor uncertainties. The breakdown of the correction factor uncertainties are shown for the $p_T^{\gamma\gamma}$ and the $N_{b\text{-jets}}$ distributions in (c) and (d), respectively.

9.6 Compatibility of measured distributions with the Standard Model

The compatibility between the measured differential distributions and the SM prediction is assessed using a χ^2 test. Table 8 reports the p -values of the χ^2 between data and the default MC prediction introduced in Section 9.3 for all differential distributions. The χ^2 is computed using the full set of uncertainties on data as well as the theory uncertainties on the SM prediction.

Distribution	$p(\chi^2)$ with Default MC Prediction
$p_T^{\gamma\gamma}$	31%
$ y_{\gamma\gamma} $	56%
$p_T^{j_1}$	88%
$N_{b\text{-jets}}$	84%

Table 8: Probabilities from a χ^2 compatibility test comparing data and the default SM prediction for each differential distribution. The χ^2 is computed using the full set of uncertainties on data and the theory uncertainties on the SM prediction.

10 Conclusions

Properties of the Higgs boson are measured in the diphoton decay channel using 79.8 fb^{-1} of pp collision data recorded by the ATLAS detector at $\sqrt{s} = 13 \text{ TeV}$. Measurements of production cross sections and phase-space measurements of simplified template cross sections are reported for a Higgs boson with $|y_H| < 2.5$. The measurements of the gluon–gluon fusion, VBF, VH , and $t\bar{t}H$ production mode cross sections, and the 9 measurements of regions defined in the framework of the simplified template cross sections, are all compatible with the Standard Model predictions.

The inclusive cross section of the Higgs boson decaying to two photons defined in a phase space that closely matches the detector acceptance and selection criteria is measured to be

$$\sigma_{\text{fid}} = 60.4 \pm 6.1 \text{ (stat.)} \pm 6.0 \text{ (exp.)} \pm 0.3 \text{ (theo.) fb},$$

which agrees with the SM prediction of $63.5 \pm 3.3 \text{ fb}$. The fiducial cross section is also measured differentially in distributions of $p_T^{\gamma\gamma}$, $|y_{\gamma\gamma}|$, and $p_T^{j_1}$. The number of b -jets produced in association with the Higgs boson is measured in a fiducial phase space requiring at least one central jet and no electrons or muons above 10 GeV. All distributions are compatible with the SM prediction. Though the precision reached with these results improve upon the previous measurement at the same center-of-mass energy, they mostly remain statistically limited.

References

- [1] ATLAS Collaboration, *The ATLAS Experiment at the CERN Large Hadron Collider*, [JINST **3** \(2008\) S08003](#).
- [2] CMS Collaboration, *The CMS experiment at the CERN LHC*, [JINST **3** \(2008\) S08004](#).
- [3] ATLAS Collaboration, *Observation of a new particle in the search for the Standard Model Higgs boson with the ATLAS detector at the LHC*, [Phys. Lett. B **716** \(2012\) 1](#), arXiv: [1207.7214 \[hep-ex\]](#).
- [4] CMS Collaboration, *Observation of a new boson at a mass of 125 GeV with the CMS experiment at the LHC*, [Phys. Lett. B **716** \(2012\) 30](#), arXiv: [1207.7235 \[hep-ex\]](#).

- [5] CMS Collaboration, *Observation of $t\bar{t}H$ production*, *Phys. Rev. Lett.* **120** (2018) 231801, arXiv: [1804.02610 \[hep-ex\]](#).
- [6] ATLAS Collaboration, *Observation of Higgs boson production in association with a top quark pair at the LHC with the ATLAS detector*, (2018), arXiv: [1806.00425 \[hep-ex\]](#).
- [7] ATLAS Collaboration, *Measurements of Higgs boson properties in the diphoton decay channel with 36 fb^{-1} of pp collision data at $\sqrt{s} = 13\text{ TeV}$ with the ATLAS detector*, (2018), arXiv: [1802.04146 \[hep-ex\]](#).
- [8] CMS Collaboration, *Measurements of Higgs boson properties in the diphoton decay channel in proton-proton collisions at $\sqrt{s} = 13\text{ TeV}$* , (2018), arXiv: [1804.02716 \[hep-ex\]](#).
- [9] LHC Higgs Cross Section Working Group (D. de Florian et al.), *Handbook of LHC Higgs Cross Sections: 4. Deciphering the Nature of the Higgs Sector*, 2016, arXiv: [1610.07922 \[hep-ph\]](#).
- [10] J. R. Andersen et al., *Les Houches 2015: Physics at TeV Colliders Standard Model Working Group Report*, 2016, arXiv: [1605.04692 \[hep-ph\]](#).
- [11] ATLAS IBL Collaboration, *Production and Integration of the ATLAS Insertable B-Layer*, *JINST* **13** (2018) T05008, arXiv: [1803.00844 \[physics.ins-det\]](#).
- [12] ATLAS Collaboration, *Performance of the ATLAS Trigger System in 2015*, *Eur. Phys. J. C* **77** (2017) 317, arXiv: [1611.09661 \[hep-ex\]](#).
- [13] K. Hamilton, P. Nason, E. Re and G. Zanderighi, *NNLOPS simulation of Higgs boson production*, *JHEP* **10** (2013) 222, arXiv: [1309.0017 \[hep-ph\]](#).
- [14] P. Nason, *A New method for combining NLO QCD with shower Monte Carlo algorithms*, *JHEP* **11** (2004) 040, arXiv: [hep-ph/0409146](#).
- [15] S. Frixione, P. Nason and C. Oleari, *Matching NLO QCD computations with parton shower simulations: the POWHEG method*, *JHEP* **11** (2007) 070, arXiv: [0709.2092 \[hep-ph\]](#).
- [16] S. Alioli, P. Nason, C. Oleari and E. Re, *A general framework for implementing NLO calculations in shower Monte Carlo programs: the POWHEG BOX*, *JHEP* **06** (2010) 043, arXiv: [1002.2581 \[hep-ph\]](#).
- [17] P. Nason and C. Oleari, *NLO Higgs boson production via vector-boson fusion matched with shower in POWHEG*, *JHEP* **02** (2010) 037, arXiv: [0911.5299 \[hep-ph\]](#).
- [18] K. Mimasu, V. Sanz and C. Williams, *Higher order QCD predictions for associated Higgs production with anomalous couplings to gauge bosons*, *JHEP* **08** (2016) 039, arXiv: [1512.02572 \[hep-ph\]](#).
- [19] J. M. Campbell et al., *NLO Higgs boson production plus one and two jets using the POWHEG BOX, MadGraph4 and MCFM*, *JHEP* **07** (2012) 092, arXiv: [1202.5475 \[hep-ph\]](#).
- [20] G. Luisoni, P. Nason, C. Oleari and F. Tramontano, *$HW^\pm/HZ + 0$ and 1 jet at NLO with the POWHEG BOX interfaced to GoSam and their merging within MiNLO*, *JHEP* **10** (2013) 083, arXiv: [1306.2542 \[hep-ph\]](#).

- [21] J. Butterworth et al., *PDF4LHC recommendations for LHC Run II*, *J. Phys. G* **43** (2016) 023001, arXiv: [1510.03865 \[hep-ph\]](#).
- [22] T. Sjöstrand, S. Mrenna and P. Z. Skands, *PYTHIA 6.4 physics and manual*, *JHEP* **05** (2006) 026, arXiv: [hep-ph/0603175](#).
- [23] T. Sjöstrand, S. Mrenna and P. Z. Skands, *A brief introduction to PYTHIA 8.1*, *Comput. Phys. Commun.* **178** (2008) 852, arXiv: [0710.3820 \[hep-ph\]](#).
- [24] ATLAS Collaboration, *Measurement of the Z/γ^* boson transverse momentum distribution in pp collisions at $\sqrt{s} = 7$ TeV with the ATLAS detector*, *JHEP* **09** (2014) 145, arXiv: [1406.3660 \[hep-ex\]](#).
- [25] J. Alwall et al., *The automated computation of tree-level and next-to-leading order differential cross sections, and their matching to parton shower simulations*, *JHEP* **07** (2014) 079, arXiv: [1405.0301 \[hep-ph\]](#).
- [26] H.-L. Lai et al., *New parton distributions for collider physics*, *Phys. Rev. D* **82** (2010) 074024, arXiv: [1007.2241 \[hep-ph\]](#).
- [27] ATLAS Collaboration, *ATLAS Pythia 8 tunes to 7 TeV data*, ATL-PHYS-PUB-2014-021, 2014, URL: <https://cds.cern.ch/record/1966419>.
- [28] S. Gieseke, A. Ribon, M. H. Seymour, P. Stephens and B. Webber, *Herwig++ 1.0: an event generator for $e^+ e^-$ annihilation*, *JHEP* **02** (2004) 005, arXiv: [hep-ph/0311208](#).
- [29] J. Bellm et al., *Herwig++ 2.7 Release Note*, 2013, arXiv: [1310.6877 \[hep-ph\]](#).
- [30] M. Bahr et al., *Herwig++ physics and manual*, *Eur. Phys. J. C* **58** (2008) 639, arXiv: [0803.0883 \[hep-ph\]](#).
- [31] GEANT4 Collaboration, *GEANT4: a simulation toolkit*, *Nucl. Instrum. Meth. A* **506** (2003) 250.
- [32] C. Anastasiou, C. Duhr, F. Dulat, F. Herzog and B. Mistlberger, *Higgs Boson Gluon-Fusion Production in QCD at Three Loops*, *Phys. Rev. Lett.* **114** (2015) 212001, arXiv: [1503.06056 \[hep-ph\]](#).
- [33] C. Anastasiou et al., *High precision determination of the gluon fusion Higgs boson cross-section at the LHC*, *JHEP* **05** (2016) 058, arXiv: [1602.00695 \[hep-ph\]](#).
- [34] S. Actis, G. Passarino, C. Sturm and S. Uccirati, *NLO electroweak corrections to Higgs boson production at hadron colliders*, *Phys. Lett. B* **670** (2008) 12, arXiv: [0809.1301 \[hep-ph\]](#).
- [35] C. Anastasiou, R. Boughezal and F. Petriello, *Mixed QCD-electroweak corrections to Higgs boson production in gluon fusion*, *JHEP* **04** (2009) 003, arXiv: [0811.3458 \[hep-ph\]](#).
- [36] M. Ciccolini, A. Denner and S. Dittmaier, *Strong and electroweak corrections to the production of Higgs + 2 jets via weak interactions at the LHC*, *Phys. Rev. Lett.* **99** (2007) 161803, arXiv: [0707.0381 \[hep-ph\]](#).
- [37] M. Ciccolini, A. Denner and S. Dittmaier, *Electroweak and QCD corrections to Higgs production via vector-boson fusion at the LHC*, *Phys. Rev. D* **77** (2008) 013002, arXiv: [0710.4749 \[hep-ph\]](#).

- [38] P. Bolzoni, F. Maltoni, S.-O. Moch and M. Zaro, *Higgs production via vector-boson fusion at NNLO in QCD*, [*Phys. Rev. Lett.* **105** \(2010\) 011801](#), arXiv: [1003.4451 \[hep-ph\]](#).
- [39] O. Brein, A. Djouadi and R. Harlander, *NNLO QCD corrections to the Higgs-strahlung processes at hadron colliders*, [*Phys. Lett. B* **579** \(2004\) 149](#), arXiv: [hep-ph/0307206](#).
- [40] L. Altenkamp, S. Dittmaier, R. V. Harlander, H. Rzehak and T. J. E. Zirke, *Gluon-induced Higgs-strahlung at next-to-leading order QCD*, [*JHEP* **02** \(2013\) 078](#), arXiv: [1211.5015 \[hep-ph\]](#).
- [41] A. Denner, S. Dittmaier, S. Kallweit and A. Mück, *Electroweak corrections to Higgs-strahlung off W/Z bosons at the Tevatron and the LHC with HAWK*, [*JHEP* **03** \(2012\) 075](#), arXiv: [1112.5142 \[hep-ph\]](#).
- [42] W. Beenakker et al., *NLO QCD corrections to $t\bar{t}H$ production in hadron collisions*, [*Nucl. Phys. B* **653** \(2003\) 151](#), arXiv: [hep-ph/0211352](#).
- [43] S. Dawson, C. Jackson, L. Orr, L. Reina and D. Wackeroth, *Associated Higgs production with top quarks at the large hadron collider: NLO QCD corrections*, [*Phys. Rev. D* **68** \(2003\) 034022](#), arXiv: [hep-ph/0305087](#).
- [44] Y. Zhang, W.-G. Ma, R.-Y. Zhang, C. Chen and L. Guo, *QCD NLO and EW NLO corrections to $t\bar{t}H$ production with top quark decays at hadron collider*, [*Phys. Lett. B* **738** \(2014\) 1](#), arXiv: [1407.1110 \[hep-ph\]](#).
- [45] S. Frixione, V. Hirschi, D. Pagani, H.-S. Shao and M. Zaro, *Electroweak and QCD corrections to top-pair hadroproduction in association with heavy bosons*, [*JHEP* **06** \(2015\) 184](#), arXiv: [1504.03446 \[hep-ph\]](#).
- [46] S. Dawson, C. Jackson, L. Reina and D. Wackeroth, *Exclusive Higgs boson production with bottom quarks at hadron colliders*, [*Phys. Rev. D* **69** \(2004\) 074027](#), arXiv: [hep-ph/0311067](#).
- [47] S. Dittmaier, M. Krämer and M. Spira, *Higgs radiation off bottom quarks at the Tevatron and the CERN LHC*, [*Phys. Rev. D* **70** \(2004\) 074010](#), arXiv: [hep-ph/0309204](#).
- [48] R. Harlander, M. Kramer and M. Schumacher, *Bottom-quark associated Higgs-boson production: reconciling the four- and five-flavour scheme approach*, 2011, arXiv: [1112.3478 \[hep-ph\]](#).
- [49] F. Demartin, F. Maltoni, K. Mawatari and M. Zaro, *Higgs production in association with a single top quark at the LHC*, [*Eur. Phys. J. C* **75** \(2015\) 267](#), arXiv: [1504.00611 \[hep-ph\]](#).
- [50] A. Djouadi, J. Kalinowski and M. Spira, *HDECAY: a program for Higgs boson decays in the Standard Model and its supersymmetric extension*, [*Comput. Phys. Commun.* **108** \(1998\) 56](#), arXiv: [hep-ph/9704448](#).
- [51] A. Djouadi, M. M. Mühlleitner and M. Spira, *Decays of supersymmetric particles: The Program SUSY-HIT (SUSpect-SdecaY-Hdecay-InTerface)*, [*Acta Phys. Polon.* **B38** \(2007\) 635](#), arXiv: [hep-ph/0609292](#).

- [52] A. Bredenstein, A. Denner, S. Dittmaier and M. M. Weber, *Radiative corrections to the semileptonic and hadronic Higgs-boson decays $H \rightarrow WW/ZZ \rightarrow 4$ fermions*, [JHEP **02** \(2007\) 080](#), arXiv: [hep-ph/0611234](#).
- [53] A. Bredenstein, A. Denner, S. Dittmaier and M. M. Weber, *Precise predictions for the Higgs-boson decay $H \rightarrow WW/ZZ \rightarrow 4$ leptons*, [Phys. Rev. D **74** \(2006\) 013004](#), arXiv: [hep-ph/0604011](#).
- [54] A. Bredenstein, A. Denner, S. Dittmaier and M. M. Weber, *Precision calculations for the Higgs decays $H \rightarrow ZZ/WW \rightarrow 4$ leptons*, [Nucl. Phys. Proc. Suppl. **160** \(2006\) 131](#), arXiv: [hep-ph/0607060](#).
- [55] T. Gleisberg et al., *Event generation with SHERPA 1.1*, [JHEP **02** \(2009\) 007](#), arXiv: [0811.4622 \[hep-ph\]](#).
- [56] S. Schumann and F. Krauss, *A Parton shower algorithm based on Catani-Seymour dipole factorisation*, [JHEP **03** \(2008\) 038](#), arXiv: [0709.1027 \[hep-ph\]](#).
- [57] S. Höche, F. Krauss, M. Schonherr and F. Siegert, *QCD matrix elements + parton showers: The NLO case*, [JHEP **04** \(2013\) 027](#), arXiv: [1207.5030 \[hep-ph\]](#).
- [58] ATLAS Collaboration, *The ATLAS Simulation Infrastructure*, [Eur. Phys. J. C **70** \(2010\) 823](#), arXiv: [1005.4568 \[physics.ins-det\]](#).
- [59] ATLAS Collaboration, *Summary of ATLAS Pythia 8 tunes*, ATL-PHYS-PUB-2012-003, 2012, URL: <https://cds.cern.ch/record/1474107>.
- [60] A. D. Martin, W. J. Stirling, R. S. Thorne and G. Watt, *Parton distributions for the LHC*, [Eur. Phys. J. C **63** \(2009\) 189](#), arXiv: [0901.0002 \[hep-ph\]](#).
- [61] ATLAS Collaboration, *Photon identification in 2015 ATLAS data*, ATL-PHYS-PUB-2016-014, 2016, URL: <https://cds.cern.ch/record/2203125>.
- [62] ATLAS Collaboration, *Electron and photon reconstruction and performance in ATLAS using a dynamical, topological cell clustering-based approach*, ATL-PHYS-PUB-2017-022, 2017, URL: <https://cds.cern.ch/record/2298955>.
- [63] ATLAS Collaboration, *Electron and photon energy calibration with the ATLAS detector using LHC Run 1 data*, [Eur. Phys. J. C **74** \(2014\) 3071](#), arXiv: [1407.5063 \[hep-ex\]](#).
- [64] ATLAS Collaboration, *Electron and photon energy calibration with the ATLAS detector using data collected in 2015 at $\sqrt{s} = 13$ TeV*, ATL-PHYS-PUB-2016-015, 2016, URL: <https://cds.cern.ch/record/2203514>.
- [65] ATLAS Collaboration, *Measurement of the photon identification efficiencies with the ATLAS detector using LHC Run-1 data*, (2016), arXiv: [1606.01813 \[hep-ex\]](#).
- [66] ATLAS Collaboration, *Measurement of the inclusive isolated prompt photon cross section in pp collisions at $\sqrt{s} = 7$ TeV with the ATLAS detector*, [Phys. Rev. D **83** \(2011\) 052005](#), arXiv: [1012.4389 \[hep-ex\]](#).
- [67] ATLAS Collaboration, *Measurement of Higgs boson production in the diphoton decay channel in pp collisions at center-of-mass energies of 7 and 8 TeV with the ATLAS detector*, [Phys. Rev. D **90** \(2014\) 112015](#), arXiv: [1408.7084 \[hep-ex\]](#).

- [68] ATLAS Collaboration, *Measurement of the Higgs boson production cross section at 7, 8 and 13 TeV center-of-mass energies in the $H \rightarrow \gamma\gamma$ channel with the ATLAS detector*, ATLAS-CONF-2015-060, 2015, URL: <https://cds.cern.ch/record/2114826>.
- [69] ATLAS Collaboration, *Topological cell clustering in the ATLAS calorimeters and its performance in LHC Run 1*, *Eur. Phys. J. C* **77** (2017) 490, arXiv: [1603.02934 \[hep-ex\]](#).
- [70] ATLAS Collaboration, *Tagging and suppression of pileup jets with the ATLAS detector*, ATLAS-CONF-2014-018, 2014, URL: <https://cds.cern.ch/record/1700870>.
- [71] ATLAS Collaboration, *Performance of pile-up mitigation techniques for jets in pp collisions at $\sqrt{s} = 8$ TeV using the ATLAS detector*, *Eur. Phys. J. C* **76** (2016) 581, arXiv: [1510.03823 \[hep-ex\]](#).
- [72] ATLAS Collaboration, *Expected performance of the ATLAS b-tagging algorithms in Run-2*, ATL-PHYS-PUB-2015-022, 2015, URL: <https://cds.cern.ch/record/2037697>.
- [73] ATLAS Collaboration, *Measurements of b-jet tagging efficiency with the ATLAS detector using $t\bar{t}$ events at $\sqrt{s} = 13$ TeV*, (2018), arXiv: [1805.01845 \[hep-ex\]](#).
- [74] ATLAS Collaboration, *Electron efficiency measurements with the ATLAS detector using 2012 LHC proton–proton collision data*, *Eur. Phys. J. C* **77** (2017) 195, arXiv: [1612.01456 \[hep-ex\]](#).
- [75] ATLAS Collaboration, *Electron efficiency measurements with the ATLAS detector using the 2015 LHC proton–proton collision data*, ATLAS-CONF-2016-024, 2016, URL: <https://cds.cern.ch/record/2157687>.
- [76] ATLAS Collaboration, *Muon reconstruction performance of the ATLAS detector in proton–proton collision data at $\sqrt{s} = 13$ TeV*, *Eur. Phys. J. C* **76** (2016) 292, arXiv: [1603.05598 \[hep-ex\]](#).
- [77] ATLAS Collaboration, *Performance of missing transverse momentum reconstruction with the ATLAS detector using proton-proton collisions at $\sqrt{s} = 13$ TeV*, (2018), arXiv: [1802.08168 \[hep-ex\]](#).
- [78] M. Oreglia, ‘A Study of the Reactions $\psi' \rightarrow \gamma\gamma\psi'$ ’, PhD thesis: SLAC, 1980, URL: <http://www-public.slac.stanford.edu/sciDoc/docMeta.aspx?slacPubNumber=slac-r-236.html>.
- [79] ATLAS Collaboration, *Search for Scalar Diphoton Resonances in the Mass Range 65–600 GeV with the ATLAS Detector in pp Collision Data at $\sqrt{s} = 8$ TeV*, *Phys. Rev. Lett.* **113** (2014) 171801, arXiv: [1407.6583 \[hep-ex\]](#).
- [80] ATLAS Collaboration, *Measurement of the isolated diphoton cross section in pp collisions at $\sqrt{s} = 7$ TeV with the ATLAS detector*, *Phys. Rev. D* **85** (2012) 012003, arXiv: [1107.0581 \[hep-ex\]](#).
- [81] G. Cowan, K. Cranmer, E. Gross and O. Vitells, *Asymptotic formulae for likelihood-based tests of new physics*, *Eur. Phys. J. C* **71** (2011) 1554, arXiv: [1007.1727 \[physics.data-an\]](#), Erratum: *Eur. Phys. J. C* **73** (2013) 2501.
- [82] ATLAS Collaboration, *Electron and photon energy calibration with the ATLAS detector using LHC Run 1 data*, *Eur. Phys. J. C* **74** (2014) 3071, arXiv: [1407.5063 \[hep-ex\]](#).

- [83] ATLAS and CMS Collaborations, *Combined Measurement of the Higgs Boson Mass in pp Collisions at $\sqrt{s} = 7$ and 8 TeV with the ATLAS and CMS Experiments*, *Phys. Rev. Lett.* **114** (2015) 191803, arXiv: 1503.07589 [hep-ex].
- [84] ATLAS Collaboration, *Luminosity determination in pp collisions at $\sqrt{s} = 8$ TeV using the ATLAS detector at the LHC*, *Eur. Phys. J. C* **76** (2016) 653, arXiv: 1608.03953 [hep-ex].
- [85] ATLAS Collaboration, *Jet energy scale measurements and their systematic uncertainties in proton–proton collisions at $\sqrt{s} = 13$ TeV with the ATLAS detector*, *Phys. Rev. D* **96** (2017) 072002, arXiv: 1703.09665 [hep-ex].
- [86] ATLAS Collaboration, *Jet Calibration and Systematic Uncertainties for Jets Reconstructed in the ATLAS Detector at $\sqrt{s} = 13$ TeV*, ATLAS-PHYS-PUB-2015-015 (2015), URL: <https://cds.cern.ch/record/2037613>.
- [87] ATLAS Collaboration, *Performance of b-jet identification in the ATLAS experiment*, *JINST* **11** (2016) P04008, arXiv: 1512.01094 [hep-ex].
- [88] X. Liu and F. Petriello, *Reducing theoretical uncertainties for exclusive Higgs-boson plus one-jet production at the LHC*, *Phys. Rev. D* **87** (2013) 094027, arXiv: 1303.4405 [hep-ph].
- [89] I. W. Stewart, F. J. Tackmann, J. R. Walsh and S. Zuberi, *Jet p_T Resummation in Higgs Production at NNLL' + NNLO*, *Phys. Rev. D* **89** (2014) 054001, arXiv: 1307.1808 [hep-ph].
- [90] R. Boughezal, X. Liu, F. Petriello, F. J. Tackmann and J. R. Walsh, *Combining resummed Higgs predictions across jet bins*, *Phys. Rev. D* **89** (2014) 074044, arXiv: 1312.4535 [hep-ph].
- [91] I. W. Stewart and F. J. Tackmann, *Theory uncertainties for Higgs and other searches using jet bins*, *Phys. Rev. D* **85** (2012) 034011, arXiv: 1107.2117 [hep-ph].
- [92] S. Gangal and F. J. Tackmann, *Next-to-leading-order uncertainties in Higgs+2 jets from gluon fusion*, *Phys. Rev. D* **87** (2013) 093008, arXiv: 1302.5437 [hep-ph].
- [93] ATLAS Collaboration, *Measurement of the Higgs boson coupling properties in the $H \rightarrow ZZ^* \rightarrow 4\ell$ decay channel at $\sqrt{s} = 13$ TeV with the ATLAS detector*, *JHEP* **03** (2018) 095, arXiv: 1712.02304 [hep-ex].
- [94] ATLAS Collaboration, *Measurements of fiducial cross-sections for $t\bar{t}$ production with one or two additional b-jets in pp collisions at $\sqrt{s} = 8$ TeV using the ATLAS detector*, *Eur. Phys. J. C* **76** (2016) 11, arXiv: 1508.06868 [hep-ex].
- [95] ATLAS Collaboration, *Measurement of differential production cross-sections for a Z boson in association with b-jets in 7 TeV proton–proton collisions with the ATLAS detector*, *JHEP* **10** (2014) 141, arXiv: 1407.3643 [hep-ex].
- [96] ATLAS Collaboration, *Measurement of the cross-section for W boson production in association with b-jets in pp collisions at $\sqrt{s} = 7$ TeV with the ATLAS detector*, *JHEP* **06** (2013) 084, arXiv: 1302.2929 [hep-ex].

- [97] ATLAS Collaboration, *Combined measurements of Higgs boson production and decay in the $H \rightarrow ZZ^* \rightarrow 4\ell$ and $H \rightarrow \gamma\gamma$ channels using $\sqrt{s} = 13$ TeV proton–proton collision data collected with the ATLAS experiment*, ATLAS-CONF-2017-047, 2017, URL: <https://cds.cern.ch/record/2273854>.
- [98] T. Chen and C. Guestrin, *XGBoost: A Scalable Tree Boosting System*, arXiv: [1603.02754 \[cs.LG\]](#).
- [99] X. Chen et al., *Precise QCD Description of the Higgs Boson Transverse Momentum Spectrum*, (2018), arXiv: [1805.00736 \[hep-ph\]](#).
- [100] M. A. Ebert, J. K. L. Michel and F. J. Tackmann, *Resummation improved rapidity spectrum for gluon fusion Higgs production*, *JHEP* **05** (2017) 088, arXiv: [1702.00794 \[hep-ph\]](#).
- [101] M. A. Ebert et al., *SCETlib: A C++ Package for Numerical Calculations in QCD and Soft-Collinear Effective Theory*, DESY-17-099, URL: <http://scetlib.desy.de>.
- [102] R. Boughezal et al., *Color singlet production at NNLO in MCFM*, *Eur. Phys. J. C* **77** (2017) 7, arXiv: [1605.08011 \[hep-ph\]](#).
- [103] J. Gaunt, M. Stahlhofen, F. J. Tackmann and J. R. Walsh, *N-jettiness Subtractions for NNLO QCD calculations*, *JHEP* **09** (2015) 058, arXiv: [1505.04794 \[hep-ph\]](#).
- [104] X. Chen, T. Gehrmann, E. W. N. Glover and M. Jaquier, *Precise QCD predictions for the production of Higgs + jet final states*, *Phys. Lett. B* **740** (2015) 147, arXiv: [1408.5325 \[hep-ph\]](#).
- [105] X. Chen, J. Cruz-Martinez, T. Gehrmann, E. W. N. Glover and M. Jaquier, *NNLO QCD corrections to Higgs boson production at large transverse momentum*, *JHEP* **10** (2016) 066, arXiv: [1607.08817 \[hep-ph\]](#).

Appendix

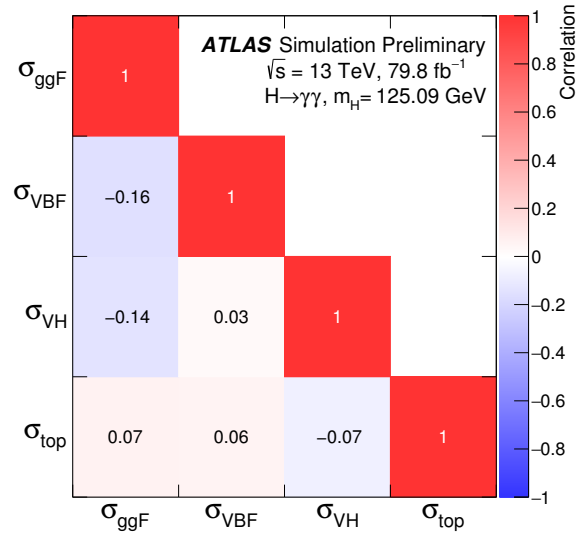


Figure 15: Expected correlations between the ggF, VBF, VH and top-associated production mode measurements, including both the statistical and systematic uncertainties.

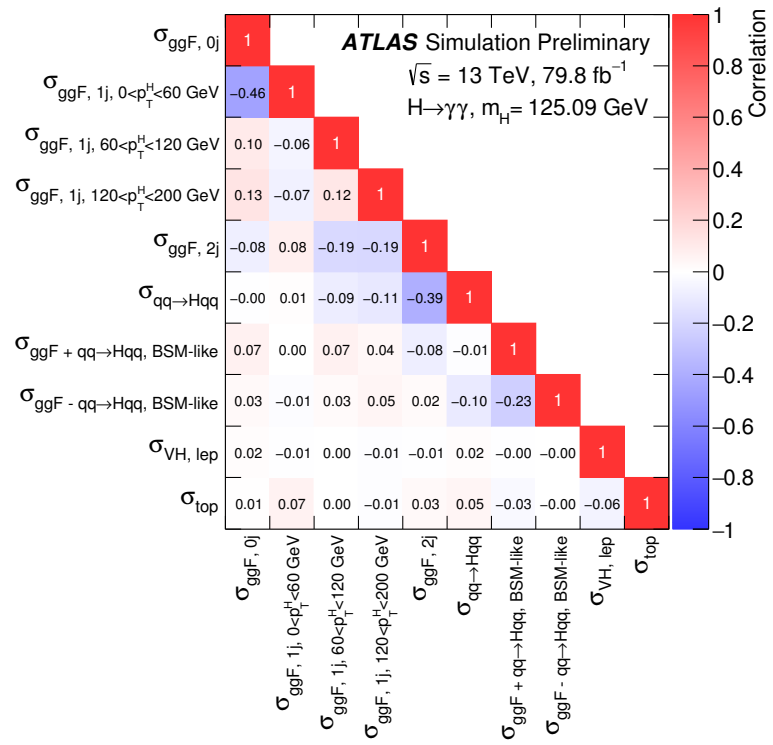


Figure 16: Expected correlations between the measured simplified template cross section regions, including both the statistical and systematic uncertainties.

Category	N_H	Efficiency [%]								
		ggF	VBF	WH	$q\bar{q}' \rightarrow ZH$	$gg \rightarrow ZH$	$t\bar{t}H$	$b\bar{b}H$	tHq	tHW
ggF 0J Cen	700	8.5	1.2	1.5	2.0	0.8	nil	10.2	nil	0.1
ggF 0J Fwd	1200	14.9	2.3	3.2	4.0	1.3	nil	16.8	0.1	0.1
ggF 1J Low	620	7.1	5.5	4.9	4.6	1.2	0.1	7.5	0.5	0.2
ggF 1J Med	330	3.4	6.1	4.1	4.1	2.6	0.1	1.9	0.7	0.3
ggF 1J High	69	0.7	1.9	1.1	1.1	2.3	0.1	0.2	0.3	0.1
ggF 1J BSM	18	0.2	0.6	0.4	0.3	0.5	nil	0.1	0.1	0.1
ggF 2J Low	180	1.8	2.6	3.5	4.0	1.9	1.9	2.3	4.2	1.9
ggF 2J Med	150	1.5	3.0	3.2	3.3	4.3	1.9	1.0	4.9	2.1
ggF 2J High	64	0.6	1.3	1.3	1.3	3.8	0.8	0.2	2.0	1.2
ggF 2J BSM	16	0.1	0.3	0.3	0.3	1.5	0.3	nil	0.5	0.6
VBF low- p_T^{Hjj} BDT loose	41	0.2	4.2	0.1	0.1	0.1	nil	0.1	0.4	nil
VBF low- p_T^{Hjj} BDT tight	29	nil	4.0	nil	nil	0.1	nil	nil	0.3	nil
VBF high- p_T^{Hjj} BDT loose	38	0.3	1.4	0.4	0.4	1.0	0.2	0.3	1.8	0.4
VBF high- p_T^{Hjj} BDT tight	46	0.3	3.4	0.3	0.3	1.3	0.3	0.2	4.3	0.4
VH had BDT loose	34	0.3	0.3	2.3	2.5	3.6	0.4	0.2	0.7	0.7
VH had BDT tight	26	0.2	0.1	2.8	2.8	5.2	0.3	0.1	0.3	0.7
qqH BSM	42	0.3	1.8	1.3	1.3	2.7	1.4	0.3	2.8	3.2
VH MET Low	1.4	nil	nil	0.2	0.5	1.0	nil	nil	nil	nil
VH MET High	2.7	nil	nil	0.3	1.1	2.3	0.1	nil	0.1	0.4
VH lep Low	12	nil	nil	4.0	0.7	0.7	1.1	0.1	2.3	2.0
VH lep High	3.1	nil	nil	1.1	0.1	0.2	0.5	nil	0.3	1.3
VH dilep	1.8	nil	nil	nil	1.2	1.5	nil	nil	nil	nil
ttH had BDT4	6.6	nil	nil	0.2	0.4	0.9	3.7	0.1	3.5	3.2
ttH had BDT3	7.2	nil	nil	0.1	0.2	0.7	5.8	0.1	2.5	4.7
ttH had BDT2	4.5	nil	nil	nil	0.1	0.3	4.3	nil	1.0	3.7
ttH had BDT1	5.2	nil	nil	nil	nil	0.2	5.3	nil	0.7	5.5
ttH lep BDT3	1.2	nil	nil	nil	nil	nil	1.0	nil	1.5	1.1
ttH lep BDT2	2.8	nil	nil	nil	nil	nil	2.8	nil	1.2	2.5
ttH lep BDT1	5.3	nil	nil	nil	nil	nil	5.6	nil	0.6	5.3
Total efficiency [%]		40.4	39.9	36.6	36.7	42.0	38.0	41.8	37.7	41.8

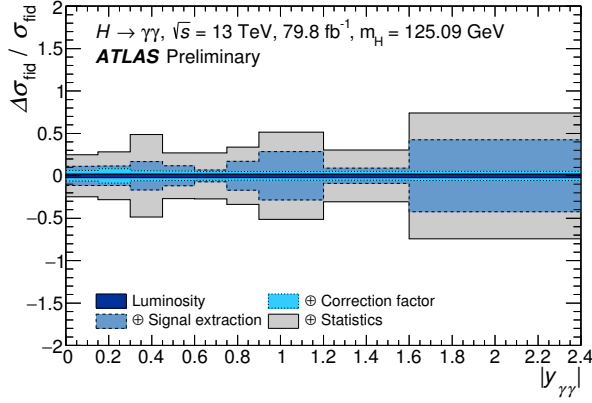
Table 9: Signal efficiencies times acceptance for each Higgs boson production mode at $\sqrt{s} = 13$ TeV, assuming $m_H = 125.09$ GeV and requiring $|y_H| < 2.5$. The signal efficiency times acceptance is reported for each category, and the last row shows the total efficiency per production process summed over the categories. Values labeled as 'nil' correspond to efficiencies that are smaller than 0.05%. The total predicted SM efficiency combining all production modes is 40.2%. The number of expected signal events, N_H , corresponds to an integrated luminosity of 79.8 fb^{-1} .

Category	N_H	Composition [%]								
		ggF	VBF	WH	$q\bar{q}' \rightarrow ZH$	$gg \rightarrow ZH$	$t\bar{t}H$	$b\bar{b}H$	tHq	tHW
ggF 0J Cen	700	97.3	0.5	0.5	0.3	nil	nil	1.4	nil	nil
ggF 0J Fwd	1200	97.2	0.6	0.5	0.4	nil	nil	1.3	nil	nil
ggF 1J Low	620	93.4	2.7	1.7	0.9	nil	nil	1.2	nil	nil
ggF 1J Med	330	88.8	6.0	2.8	1.6	0.2	nil	0.6	nil	nil
ggF 1J High	69	83.4	9.2	3.9	2.2	0.8	0.1	0.3	0.1	nil
ggF 1J BSM	18	81.3	10.3	4.9	2.3	0.7	0.1	0.3	0.1	nil
ggF 2J Low	180	85.4	4.4	4.4	2.9	0.2	1.1	1.3	0.3	nil
ggF 2J Med	150	83.4	6.0	4.7	2.8	0.6	1.3	0.7	0.4	nil
ggF 2J High	64	82.5	6.3	4.8	2.8	1.4	1.3	0.4	0.4	0.1
ggF 2J BSM	16	82.3	5.1	5.1	2.8	2.1	1.8	0.2	0.4	0.1
VBF low- p_T^{Hjj} BDT loose	41	51.8	46.5	0.6	0.4	0.1	0.1	0.4	0.2	nil
VBF low- p_T^{Hjj} BDT tight	29	23.4	75.8	0.2	0.1	0.1	nil	0.1	0.3	nil
VBF high- p_T^{Hjj} BDT loose	38	81.5	11.7	2.4	1.5	0.7	0.7	0.8	0.7	nil
VBF high- p_T^{Hjj} BDT tight	46	65.1	28.6	1.7	1.0	0.8	0.7	0.5	1.6	nil
VH had BDT loose	34	69.2	2.5	14.8	9.2	2.3	1.3	0.4	0.3	0.1
VH had BDT tight	26	53.8	1.7	24.3	13.9	4.5	1.3	0.2	0.2	0.1
qqH BSM	42	65.9	14.8	7.5	4.3	1.6	3.9	0.8	1.0	0.2
VH MET Low	1.4	16.4	0.5	23.1	44.3	15.0	0.5	nil	0.2	nil
VH MET High	2.7	1.3	nil	25.0	49.5	18.2	5.2	nil	0.4	0.4
VH lep Low	12	9.7	0.5	69.6	6.6	1.2	8.9	0.7	2.3	0.4
VH lep High	3.1	0.1	0.1	76.8	3.7	1.4	15.6	nil	1.2	1.2
VH dilep	1.8	nil	nil	nil	80.8	17.8	1.4	nil	nil	nil
ttH had BDT4	6.6	22.3	1.5	5.1	6.0	2.8	53.5	1.5	6.1	1.2
ttH had BDT3	7.2	10.9	0.6	2.5	3.2	1.9	74.7	0.7	3.8	1.6
ttH had BDT2	4.5	5.2	0.3	1.2	1.7	1.1	85.7	0.4	2.4	2.0
ttH had BDT1	5.2	2.2	0.1	0.7	1.0	0.6	91.2	0.2	1.4	2.6
ttH lep BDT3	1.2	0.8	nil	5.4	1.9	0.7	75.7	0.1	13.1	2.2
ttH lep BDT2	2.8	nil	nil	1.8	0.5	0.2	90.3	nil	4.9	2.2
ttH lep BDT1	5.3	0.1	nil	0.5	0.2	0.1	95.4	nil	1.3	2.5

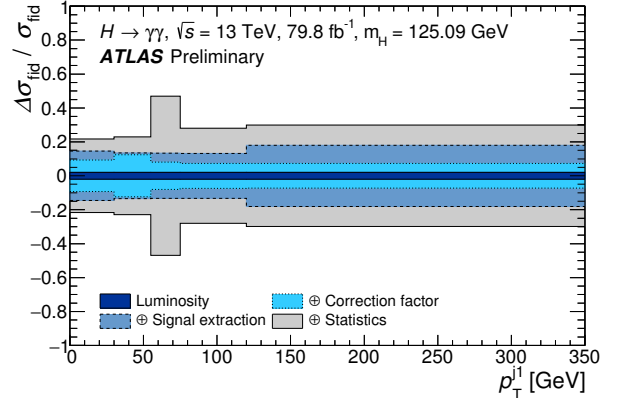
Table 10: Composition of the selected Higgs boson events, in terms of the different production modes, as expected for each reconstructed category. Values labeled as 'nil' correspond to efficiencies that are smaller than 0.05%. The total number of expected signal events, N_H , corresponds to an integrated luminosity of 79.8 fb^{-1} .

Category	σ_{68} [GeV]	σ_{90} [GeV]	S_{90}	B_{90}	f_{90}	Z_{90}
ggF 0J Cen	1.7	3.0	630	13 000	0.1	5.6
ggF 0J Fwd	2.1	3.8	1100	46 000	0.0	5.2
ggF 1J Low	1.9	3.6	560	19 000	0.0	4.0
ggF 1J Med	1.8	3.4	300	6900	0.0	3.6
ggF 1J High	1.7	3.1	62	640	0.1	2.4
ggF 1J BSM	1.4	2.7	16	80	0.2	1.8
ggF 2J Low	2.0	3.6	160	7700	0.0	1.9
ggF 2J Med	1.9	3.4	140	4100	0.0	2.1
ggF 2J High	1.7	3.1	57	690	0.1	2.2
ggF 2J BSM	1.5	2.8	14	61	0.2	1.7
VBF low- p_T^{Hjj} BDT loose	1.9	3.5	37	280	0.1	2.2
VBF low- p_T^{Hjj} BDT tight	1.7	3.1	26	35	0.4	4.0
VBF high- p_T^{Hjj} BDT loose	1.8	3.5	34	690	0.1	1.3
VBF high- p_T^{Hjj} BDT tight	1.7	3.2	41	320	0.1	2.3
VH had BDT loose	1.8	3.2	31	470	0.1	1.4
VH had BDT tight	1.6	2.9	23	110	0.2	2.1
qqH BSM	1.5	2.8	38	610	0.1	1.5
VH MET Low	1.9	3.6	1.3	9.8	0.1	0.4
VH MET High	1.6	3.0	2.4	6.5	0.3	0.9
VH lep Low	1.9	3.4	11	95	0.1	1.1
VH lep High	1.5	3.0	2.8	5.3	0.3	1.1
VH dilep	1.7	3.2	1.6	2.6	0.4	0.9
ttH had BDT4	1.7	3.2	6.1	55	0.1	0.8
ttH had BDT3	1.7	3.2	6.7	33	0.2	1.1
ttH had BDT2	1.6	3.1	4.1	8.2	0.3	1.4
ttH had BDT1	1.4	2.7	4.8	1.4	0.8	3.0
ttH lep BDT3	1.9	3.5	1.1	4.7	0.2	0.5
ttH lep BDT2	1.8	3.3	2.5	4.9	0.3	1.1
ttH lep BDT1	1.6	3.0	4.8	2.2	0.7	2.6

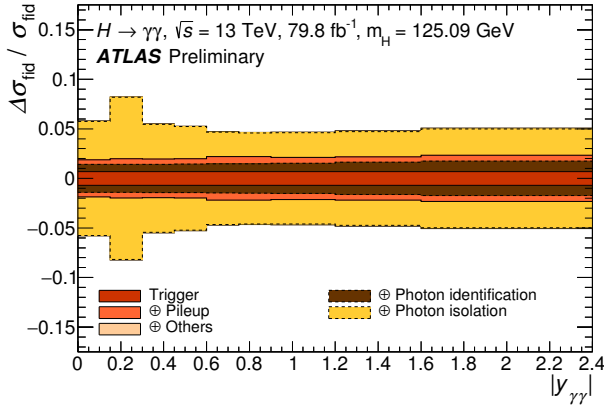
Table 11: The effective signal mass resolutions σ_{68} (σ_{90}) in GeV defined as half the width containing 68% (90%) of the signal events listed for each reconstructed category. Further, the numbers of background events B_{90} , measured by fits to the data, in the smallest interval expected to contain 90% of the SM signal events S_{90} are given, accompanied by the expected purities $f_{90} \equiv S_{90}/(S_{90} + B_{90})$ and expected significances $Z_{90} \equiv \sqrt{2((S_{90} + B_{90}) \log(1 + S_{90}/B_{90}) - S_{90})}$.



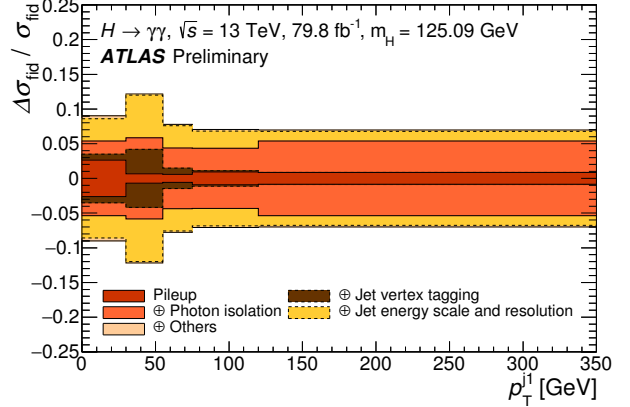
(a)



(b)



(c)



(d)

Figure 17: The systematic uncertainties, relative to the differential cross sections measured in data, in each bin of (a) the $|y_{\gamma\gamma}|$ and (b) the p_T^{j1} differential distributions, sequentially summed in quadrature. The systematic uncertainty is composed of luminosity, signal extraction and correction factor uncertainties. The breakdown of the correction factor uncertainties are shown for the $|y_{\gamma\gamma}|$ and the p_T^{j1} distributions in (c) and (d), respectively.